

# A large language model-type architecture for high-dimensional molecular potential energy surfaces

Xiao Zhu, Srinivasan S. Iyengar,<sup>1</sup>

<sup>1</sup>*Department of Chemistry, Department of Physics,  
and the Indiana University Quantum Science and Engineering Center (IU-QSEC),  
Indiana University, 800 E. Kirkwood Ave, Bloomington, IN-47405*

(Dated: December 6, 2024)

Computing high dimensional potential surfaces for molecular and materials systems is considered to be a great challenge in computational chemistry with potential impact in a range of areas including fundamental prediction of reaction rates. In this paper we design and discuss an algorithm that has similarities to large language models in generative AI and natural language processing. Specifically, we represent a molecular system as a graph which contains a set of nodes, edges, faces etc. Interactions between these sets, which represent molecular subsystems in our case, are used to construct the potential energy surface for a reasonably sized chemical system with 51 dimensions. Essentially a family of neural networks that pertain to the graph-based subsystems, get the job done for this 51 dimensional system. We then ask if this same family of lower-dimensional neural networks can be transformed to provide accurate predictions for a 186 dimensional potential surface. We find that our algorithm does provide reasonably accurate results for this larger dimensional problem with sub-kcal/mol accuracy for the higher dimensional potential surface problem.

## I. INTRODUCTION

The problem of computing accurate post-Hartree-Fock potential energy surfaces for large chemical systems is considered to be an exponentially complex task in quantum chemistry. However, computing such accurate potentials is essential for a range of problems that include not only the fundamental description of chemical reactions and molecular vibrations[1–8], but also topics such as the design of new molecular assemblies with desired properties [9–13]. The complexity of describing all such phenomena is governed by the following fundamental limitations. As the system size grows, the number of nuclear dimensions grow. For  $\mathcal{D}$  nuclear dimensions with each dimension discretized and represented using  $M$  multi-dimensional basis points where such basis-point may represent nuclear geometries, the number of such geometries grows exponentially with the number of nuclear dimensions, and the problem is thought to scale as  $O(M^{\mathcal{D}})$ . [1–3, 6, 14–23] Additionally, if post-Hartree Fock accuracy is desired, computing each potential energy may scale as  $O(N^{7-10})$ , for  $N$  electrons. Thus the problem of computing accurate potential surfaces grows as  $O(M^{\mathcal{D}} * N^{7-10})$ , which becomes intractable even for moderate sized systems.

Recently, many groups have used machine learning methods to compute accurate potential energy surfaces. [24–33] However, for obtaining multidimensional potentials, the amount of data needed to train these models could also grow steeply and additionally, when accurate electron correlation information is needed, as noted above, the training cost may be prohibitive. The complexity of obtaining such neural network(NN) models may be seen from the density of the edges on the right side of Figure 1. Here, the multi-dimensional electronic

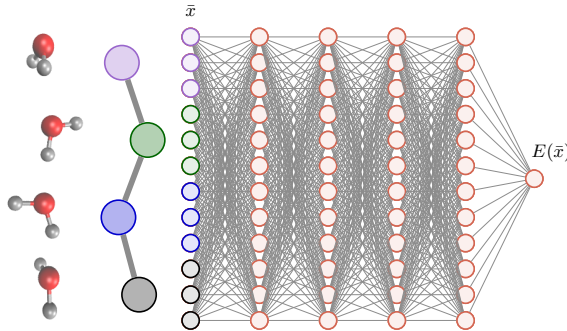


FIG. 1. The density of gray edges represents the number of network weights that need to be computed to obtain a representation of the potential surface.

potential energy surface for a simple water wire system, depicted as a graphical chain with individual water molecules shown as nodes, is extrapolated using the neural network on the right. The gray edges represent the neural network weights that need to be computed through training, and the density of such edges, represents the complexity of the training problem. Figure 1 does not account for the steep algebraic scaling needed to compute the training data (or span of  $\bar{x}$  in Figure 1) within the training set. Due to such reasons, the largest system studied to date using couple-cluster data is  $H_9O_4^+$  [26] (with absolute error of 0.09 kcal/mol), and the resultant model shows limited transferability to  $H_{13}O_6^+$  where the mean absolute error is found to be 1.32 kcal/mol [24, 34, 35]. Water clusters, of course, have received great attention here due to their broad and fundamental significance [36–46] and also due to challenges

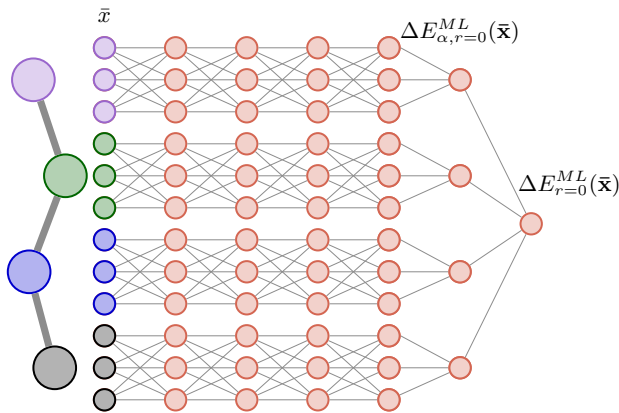


FIG. 2. Visual illustration of neural networks used to compute  $\{\Delta E_{\alpha,r}^{ML}(\bar{x})\}$  for  $r = 0$ . See Eq. (2).

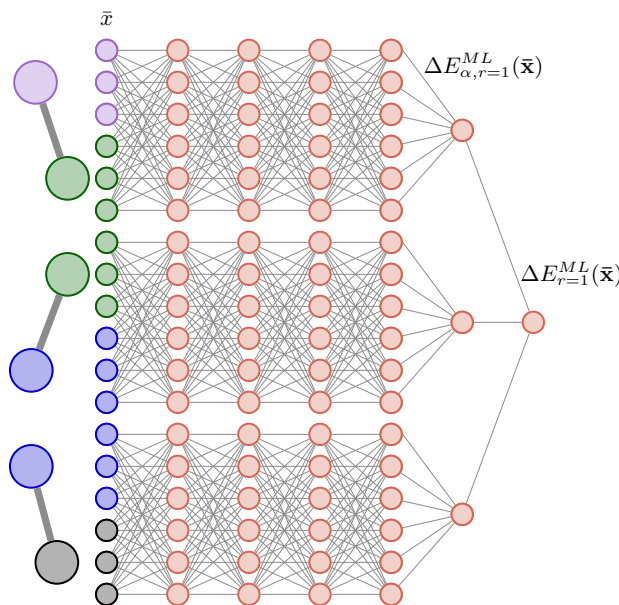


FIG. 3. Visual illustration of neural networks used to compute  $\{\Delta E_{\alpha,r}^{ML}(\bar{x})\}$  for  $r = 1$ . See Eq. (2).

posed to both experiment and theory[37–42, 44].

In this paper, we introduce a machine-learning based approach to compute multidimensional potential surfaces that we show is applicable for much larger systems than previously described. The key question we attempt to address here is whether neural networks of lower complexity, that is neural networks with fewer degrees of freedom corresponding to systems requiring fewer learning cycles and training effort, can be rigorously harnessed together to create a larger network that can be used to solve a larger problem. Towards this, we use our graph-

theoretic procedure for molecular fragmentation[47–63]. This approach may be thought of as a generalized convolution neural network[64, 65] where the convolution is dictated by the spatial proximity of groups within a molecular system which is defined through a graphical network. An example of how such a scheme works is shown in Figures 2 and 3, where the neural network in Figure 1 is visually simplified into a family of networks obtained using convolutions defined by graphical representation of the molecular system. Notice that both Figures 2 and 3 show separate neural networks each of these being far lower in complexity than that in Figure 1. These separate neural networks are then harnessed together using the topology of the graph description. In Refs. [55, 58], we have shown that this approach can be used as a graph-theory based transfer learning protocol where fragment neural networks can lead to accurate potential surfaces in higher dimensions[55, 58]. In this paper, we show that the individual models of these graph-based molecular fragments can be incrementally further improved to provide accurate results for even larger systems than they were originally parameterized. Specifically in Ref. 58, we showed how neural networks written for small water clusters such as protonated/neutral dimers and trimers can be used to compute accurate potentials with errors in the sub-kcal/mol range for a larger solvated Zundel system. Here we show how these same sets of neural networks can be further refined to obtain sub-kcal/mol accuracy for potential surfaces for even larger systems such as the protonated 21-water cluster system. Thus, in this paper, for the first time, we provide a systematic strategy to obtain accurate, coupled cluster level potentials for large dimensional systems. Here we illustrate our procedure for a 186-dimensional problem, the protonated 21-water cluster system.

## II. THEORETICAL METHODS

In order to go from the complexity in Figure 1 to that in Figures 2 and 3, we first construct a graph based molecular fragmentation of our chemical system. This graph then becomes the basis for our convolution diagram that leads to a family of decoupled neural networks. A graph  $\mathcal{G}$ , comprised of molecular fragments treated as nodes (or vertices), is defined as  $\mathcal{G} \equiv \{\mathbf{V}_0; \mathbf{V}_1\}$ . Here,  $\mathbf{V}_0$  is the set of vertices (fragments within a molecule or a cluster), and  $\mathbf{V}_1$  is the set of edges that capture interactions between these vertices and hence are larger fragments. Once such a graph is defined, higher rank objects, and hence larger fragments and molecular aggregates that represent high order interactions up to a maximum rank  $\mathcal{R}$ , are also specified by the graph as

$$\{\mathbf{V}_r | r = 0, \dots, \mathcal{R}\} \equiv \{\mathbf{V}_0, \mathbf{V}_1, \mathbf{V}_2, \dots, \mathbf{V}_r, \dots, \mathbf{V}_{\mathcal{R}}\}. \quad (1)$$

Mathematical components	Instance in Molecular potential energy surfaces	Instance in a language
Graph: Nodes	Groups of atoms or molecular fragments	Words or phrases (token) in a sentence.
Graph: Edges	Interaction between molecular fragments	Concatenated words or phrases. Sentence Grammar and semantics.
Graph: Faces	Higher order interaction between fragments	Larger language components from concatenated set of words or phrases.

FIG. 4. The common constructs of graph based depiction of molecular potential surfaces used here and elements of a large language model (LLM).

The quantity  $\mathbf{V}_r$  represents the set of all rank- $r$  entities in the graph that may be used to capture the interactions between  $(r + 1)$  molecular fragments. The post-Hartree-Fock, “*target*”, electronic potential surface may then be written using such a graph-theoretic representation as

$$E^{target}(\bar{\mathbf{x}}) = E^{Ref}(\bar{\mathbf{x}}) + \sum_{r=0}^{\mathcal{R}} \sum_{\alpha_r \in \mathbf{V}_r} \mathcal{M}_{\alpha_r, r}^{\mathcal{R}} \Delta E_{\alpha_r, r}(\bar{\mathbf{x}}) \quad (2)$$

where

$$\Delta E_{\alpha_r, r}(\bar{\mathbf{x}}) = E_{\alpha_r, r}^{target}(\bar{\mathbf{x}}) - E_{\alpha_r, r}^{Ref.}(\bar{\mathbf{x}}) \quad (3)$$

The designation, “*Ref*”, is some reference electronic structure level such as DFT at nuclear configuration  $\bar{\mathbf{x}}$ . In Eq. 2, a high-level energy correction  $\Delta E_{\alpha_r, r}(\bar{\mathbf{x}})$  for each fragment or simplex,  $\alpha_r \in \mathbf{V}_r$  is added to a reference energy, such as DFT. We further stress in Eq. 2 that it is these simplex energies that are ML-trained hence leading to the simplification from Figure 1 to Figures 2 and 3. The quantity,  $\mathcal{M}_{\alpha_r, r}$  above represents the total number of times the simplex  $\alpha_r \in \mathbf{V}_r$  appears in all simplexes with ranks greater than  $r$ . For every type of simplex, energy corrections  $\Delta E_{\alpha_r, r}(\bar{\mathbf{x}})$  are modeled using neural networks to obtain  $\Delta E_{\alpha_r, r}^{ML}(\bar{\mathbf{x}})$ .

In this publication we show that a family of neural networks used to train the quantities,  $\{\Delta E_{\alpha_r, r}(\bar{\mathbf{x}}) \rightarrow \Delta E_{\alpha_r, r}^{ML}(\bar{\mathbf{x}})\}$  and obtain an accurate potential energy surface for one system, that is  $\{\Delta E_{\alpha_r, r}^{ML}(\bar{\mathbf{x}})\} \rightarrow E_{\text{system},1}^{target}(\bar{\mathbf{x}})$ , can be refined to yield an accurate potential to a much larger system, that is,  $\{\Delta E_{\alpha_r, r}^{ML}(\bar{\mathbf{x}})\} \rightarrow E_{\text{system},2}^{target}(\bar{\mathbf{x}})$ . In this way, we provide an algorithm for growth in learning and our approach looks very similar to the “transformer” architecture used in large language models[66]. To further emphasize this connection, in Figure 4, we inspect the similarity between the mathematical model (graphs) used to represent molecular potential surfaces and basic constructs in a language. The current methodologies in natural language processing (NLP) involve mapping linguistic components such as words or phrases onto abstract vector spaces (that may be represented as nodes here in our graph description), where semantic relations between words are represented as distances

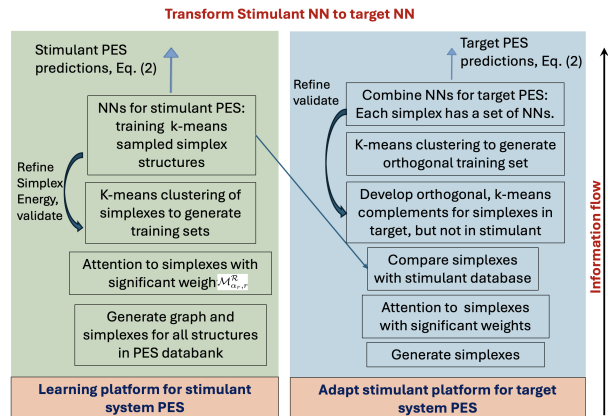


FIG. 5. General flow of data to generate a family of NNs that yield a target system potential, after these have been trained for a stimulant system potential energy surface.

(edges in graphs) between these vector representation of the primary linguistic components. This technique is used in large Generative AI models, and connections between our abstraction of molecular potential energy surfaces are presented in Figure 4. Further details on these connections are discussed in Appendix A.

Associated with these connections, our general process flow is depicted in Figure 5. The left, green panel, *encodes* the machine learning description by computing neural networks for  $\{\Delta E_{\alpha_r, r}^{ML}(\bar{\mathbf{x}})\}$  that are used to compute  $E_{\text{system},1}^{target}(\bar{\mathbf{x}})$ . The right, blue panel, then begins with this family of neural networks and then improves on it to obtain approximations for  $E_{\text{system},2}^{target}(\bar{\mathbf{x}})$ . Thus we show here that the graph-theoretic approach to construct a convolution of accurate, lower cost neural networks can be generalized to grow neural networks that are applicable to even larger systems than systems for which these neural networks were originally designed. With respect to connections to generative AI and LLM, the process here is akin to first analyzing the semantics between all possible word pairs, word triplets and word quartets in a sentence. (See Figure 4.) These word-sets may or may not be nearest neighbors. That is, we not only include 1-2 (concatenated) nearest-neighbor interactions, but also 1-3, 1-4, and so on, word-word-type interactions. Once the semantics behind all word subsets within a language component such as a sentence is understood (the equivalent of obtaining accurate  $E_{\text{system},1}^{target}(\bar{\mathbf{x}})$  values), the associated family of neural networks are tested for a larger language component such as a paragraph or an essay (the equivalent of obtaining accurate  $E_{\text{system},2}^{target}(\bar{\mathbf{x}})$  values).

As an illustration of our approach, we will show how simplex neural networks that were originally defined for obtaining accurate potential surfaces for the solvated zundel system can now be generalized to obtain results for the much larger protonated 21 water cluster. Thus,

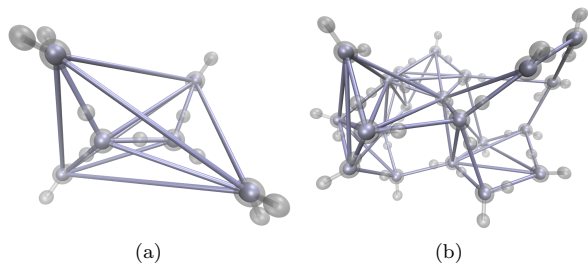


FIG. 6. The graphical complexity for the two systems.

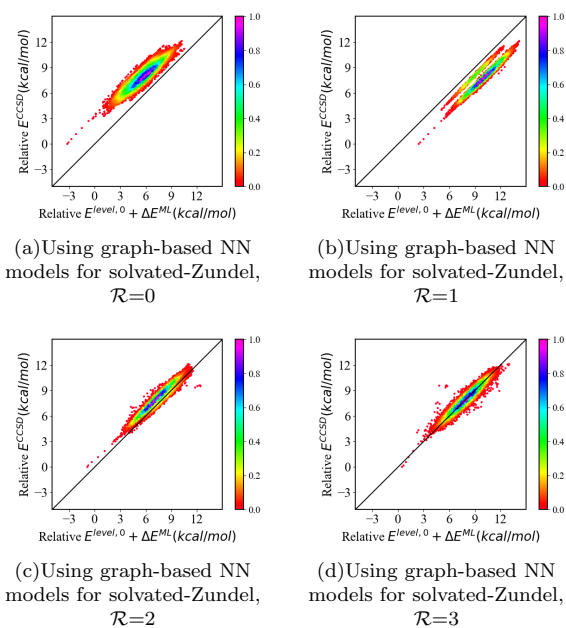


FIG. 7. The solvated zundel potential energy absolute errors.

this paper provides the first milli-Hartree level neural network description of larger protonated water clusters.

### III. RESULTS

The critical aspects of our approach can be seen in Figures 6, 7 and 8. Figure 6 is used to allude to the complexity of the graphical representation as one moves from the solvated Zundel system to the protonated 21-water cluster. Specifically, assuming  $O(N^6)$  complexity for the CCSD electronic structure values used here, each electronic structure value for the system in Figure 6(b) is 1762 times more expensive to compute than for that in Figure 6(a). When one accounts for the fact that the system in Figure 6(b) has 186 independent degrees of freedom, whereas system in Figure 6(a) contains *only* 51

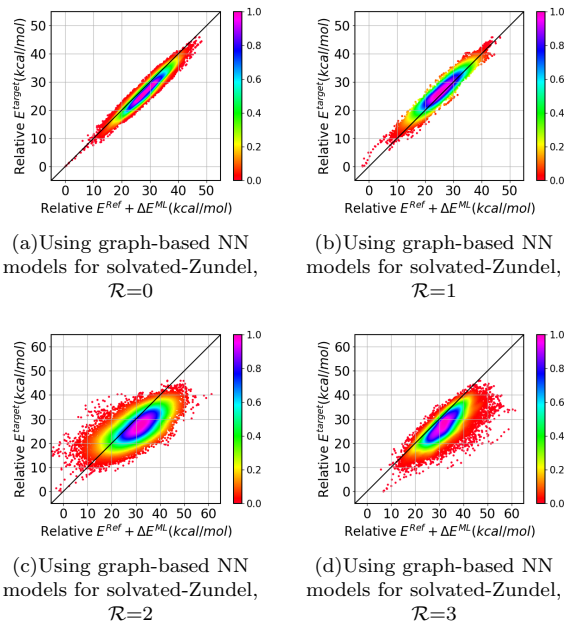


FIG. 8. The protonated 21 water cluster absolute errors from NN models obtained from solvated Zundel system. Clearly the error increases with increasing rank, since the potential surface space for the larger clusters in the 21-mer is not well-represented in the original solvated Zundel data.

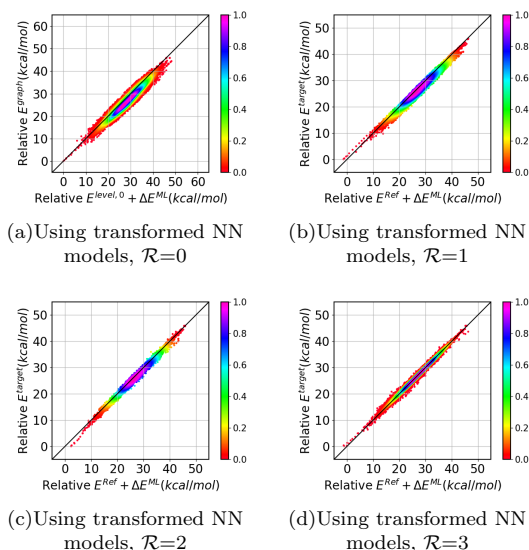


FIG. 9. The protonated 21 water cluster potential energy prediction accuracy from transformed NN models.

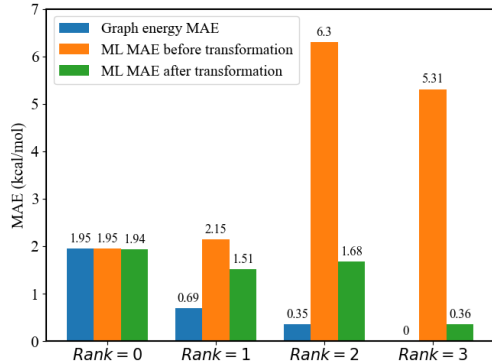


FIG. 10. Improved performance of the transformed neural networks.

degrees of freedom, the prohibitive exponential complexity associated with training for the system in Figure 6(b) is apparent.

In Figure 7, we demonstrate the behavior of the ML architectures for the solvated Zundel problem. This error (spread of the distribution away from the solid diagonal line) is given by (from Eq. (2)),

$$\begin{aligned}
 E_{ML}^{target}(\bar{\mathbf{x}}) - E^{target}(\bar{\mathbf{x}}) \\
 = \sum_{r=0}^{\mathcal{R}} \sum_{\alpha_r \in \mathbf{V}_r} \mathcal{M}_{\alpha_r, r}^{\mathcal{R}} (\Delta E_{\alpha_r, r}^{ML}(\bar{\mathbf{x}}) - \Delta E_{\alpha_r, r}(\bar{\mathbf{x}}))
 \end{aligned}
 \quad (4)$$

Clearly, the neural networks have been well-trained for solvated Zundel (see SI), however, when these same neural network models are used to compute the potential surface for the protonated 21-water cluster, one sees an increase in error with increasing values of rank,  $\mathcal{R}$ , as seen in Figure 8(a)-(d). Thus, in fact, when the primitive solvated Zundel neural network models are used, the errors get worse with increasing rank and there is a need to adapt these neural networks to data that is orthogonal to the original solvated Zundel data. We do this by modifying our neural networks for the simplexes that are already part of solvated Zundel, through an incremental k-means-based tessellation scheme on permutationally invariant descriptors of our training data. (See SI.) As a result of this incremental k-means based tessellation scheme, we improve the performance of the primitive solvated Zundel neural networks as seen in Figure 9. This aspect is further summarized in Figure 10, where it is clear that the new, modified models (green) perform substantially better than the original solvated Zundel model (orange). As a result of this modified, incremental, and directed learning process, the overall error in the protonated 21-water cluster reduces from 5.32 kcal/mol (the error when the solvated Zundel models are directly used) to 0.36 kcal/mol (when the modified, incremental,

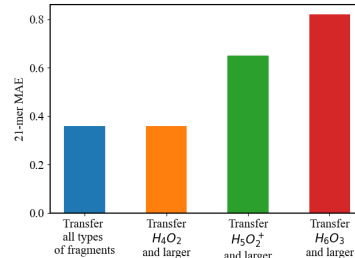


FIG. 11. The protonated 21-water cluster MAE if the transformation process is conducted only on fragments larger in size than those listed. This shows that nodes do not need to be transformed and accuracy may be maintained even when all edges are not transformed.

and directed learning process is used).

The data provided, however, modifies all neural networks. Clearly, this may not be necessary, as can be seen through the comparison of Figures 8 and 9. How do the results change if only the larger simplex neural networks are modified? We examine the potential energy predictions for the protonated 21-water cluster when the modified, incremental, directed learning process is only applied to the models for larger fragments. The error is displayed in Figure 11 where the first blue bar represents the MAE from the green bar corresponding to  $\mathcal{R}=3$  in Figure 10. As seen from comparing the blue and orange bars in Figure 11, omitting  $H_2O$  and  $H_3O^+$  fragments from the modification process leads to negligible differences in MAE. However, excluding  $H_4O_2$  results in MAE rising from 0.36 kcal/mol to 0.65 kcal/mol as shown by the green bar in Figure 11. A similar pattern can be seen when  $H_5O_2^+$  are further excluded as shown by the red bar in Figure 11. The MAE continues to rise to 0.82 kcal/mol.

#### IV. CONCLUSION

The cost of acquiring sufficient training samples to construct accurate neural network models for large system potential energy surfaces at the couple-cluster level of theories has presented a great challenge to computational chemistry. In this paper, we present a transfer learning protocol which extends from a small known (learned) system, in our case the solvated zundel system, to predict the potential energy surface for a much larger system, in our case the protonated 21-water cluster. Thus, we wish to construct learning models appropriate for a 51-dimensional space (solvated zundel) and adapt those models to extrapolate the quantum mechanical energies for a 186-dimensional space (the protonated 21-water cluster).

Towards this, we begin by using our previously devel-

oped graph-theoretic molecular fragmentation procedure for configuring common fragments from both systems. Then, we construct a set of neural network models that learn on the energies from each type of fragment separately from a solvated zundel library of structures. To better represent the graph-theoretically generated fragment geometries and understand their differences, we designed a permuted inter-atomic distance vector that follows translational, rotational, and permutation invariance as the descriptor. These neural network models provide highly accurate predictions on the solvated zundel potential energies at an MAE of 0.36 kcal/mol, but lose accuracy when directly used for predicting energies for the protonated 21-water cluster with an MAE of 5.32 kcal/mol due to the change in distribution of fragments structures. Thus, we design a modified, incremental and directed transfer learning process that first distinguishes the extent of fragment structural differences between the two systems. Once these differences are understood, an incremental learning process yields results with sub-kcal/mol accuracy of the full potential energy surface of the protonated 21-water cluster. We obtain highly accurate potential energy predictions for a protonated 21-water cluster dynamics trajectory, with MAE of 0.36 kcal/mol at CCSD level while also maintaining good accuracy for the initial solvated zundel system using the same family of neural network models.

## V. ACKNOWLEDGEMENT

This research was supported by the National Science Foundation grant CHE-2102610 to SSI. The computational facilities at Indiana University are duly acknowledged and have been critical to this effort. Acknowledgment is due in part to the Lilly Endowment, Inc., for their support of the BigRed computing facility at Indiana University widely used in the effort represented in this publication. This work was also supported in part by Shared University Research grants from IBM, Inc., to Indiana University, which supports the Scholarly Data Archives.

**Supporting Information:** In the Supporting Information section, (a) we analyze and estimate the complexity of obtaining enough training samples for constructing accurate potential energy surfaces, (b) we briefly outline our graph theory-based neural network procedure, and introduce a systematic procedure for constructing our permutation invariant interatomic distances descriptor for fragments, (c) we analyze the similarities between computing molecular potential energy surfaces and language processing from the graph representation perspective, (d) we discuss how an existing learning model can be further refined, (e) we provide more details about our mini-batch-k-means sampling method and neural network setup, (f) we show how fragment accuracy is im-

proved following our incremental learning process, and (g) summarize the cost for constructing models for potential energy surface from graph-theoretic fragmentation.

## Appendix A: Connections between computing molecular potential energy surface and natural language processing

Here we explore the connections between computing molecular potential energy surfaces and processing language components from an abstract viewpoint. Each component of a molecular system, such as a fragment, has many different possible energy values arising from multiple possible configurations, and the stability of each of these configurations is dependent on how the fragment adapts to its surroundings (as manifested through edges and faces in a graph). Likewise, parts of a sentence, such as a word or a phrase, may carry different meanings with some probabilistic distribution, and this distribution “collapses” to the intended meaning given the presence of other language components (such as surrounding words and phrases) providing a context. In our work, the weight of each molecular fragment has a critical role that arises completely from geometric considerations as enforced by graphical constraints, and allows us to compute the full system potential energy as a weighted sum of fragment energies. See Eq. (2) in the main text and Eq. (S10) in SI, and these are reproduced here for convenience:

$$E^{target}(\bar{\mathbf{x}}) - E^{Ref}(\bar{\mathbf{x}}) = \sum_{r=0}^{\mathcal{R}} \sum_{\alpha_r \in \mathbf{V}_r} \mathcal{M}_{\alpha_r, r}^{\mathcal{R}} \Delta E_{\alpha_r, r}(\bar{\mathbf{x}}) \quad (\text{A1})$$

which may be rewritten as

$$\Delta E^{Ref \rightarrow target}(\bar{\mathbf{x}}) = \sum_{r=0}^{\mathcal{R}} \sum_{\alpha_r \in \mathbf{V}_r} \mathcal{M}_{\alpha_r, r}^{\mathcal{R}} \Delta E_{\alpha_r, r}(\bar{\mathbf{x}}) \quad (\text{A2})$$

In a complementary fashion, in natural language processing, the attention mechanism within transformers[66] determines the importance, and contextual meaning of each word by analyzing the relationship between all possible pairs of words within a sentence or a paragraph. In the transformer, each word or token is embedded by three vectors: *query*, *key*, and *value*. The *query* vectors encode questions about a specific word whereas the *key* vectors contain potential maps to other known words in some dictionary. Consequently, their dot product,  $[Q_i \cdot K_j]$ , that is the dot product of the  $i$ -th *query* vector with the  $j$ -th *key* vector, produces the relevance of the  $j$ -th *key* to a certain *query*. Collecting all possible such inner products, provides a cumulative relevance of a certain *query* vector,  $[Q_i K^T]$ , where

$K^T \equiv \{K_1, K_2, \dots\}$  contains all *key* vectors. By extension, the quantity  $[QK^T]$  simply projects all *query* vectors onto the *key* vector-space. The most important idea in Ref. [66] is to scale  $[QK^T]$  using a *softmax* function,

$$\left[ \text{softmax} \left( \frac{QK^T}{\sqrt{d}} \right) \right]_{i,j} = \frac{\exp\{Q_i \cdot K_j / \sqrt{d}\}}{\sum_k \exp\{Q_i \cdot K_k / \sqrt{d}\}} \quad (\text{A3})$$

where  $d$  is the dimensionality of each *query* vector and *key* vector. Thus, the *softmax* function, in Boltzmann-style, simply weights the most significant *key* vectors that contribute to all queries. In a sense, this performs the same functionality as  $\mathcal{M}_{\alpha_r, r}^{\mathcal{R}}$  in Eq. (A2) where  $\mathcal{M}_{\alpha_r, r}^{\mathcal{R}}$  also projects out the importance of the  $\alpha_r$ -th,  $r$ -rank fragment (or simplex) (also see Eq. (S3) in SI). Hence, we may loosely state that

$$\left[ \text{softmax} \left( \frac{QK^T}{\sqrt{d}} \right) \right]_{i,j} \leftrightarrow \mathcal{M}_{\alpha_r, r}^{\mathcal{R}} \quad (\text{A4})$$

Importantly, both terms in Eq. (A4) arise from purely geometric considerations. Geometry in the context of molecule is the spatial spread of fragments, whereas geometry in the context of natural language processing is connectivity or conjunction of words or phrases.

The next important part of the transformer architecture[66] is the *value* vector space. The *key-value* pairs together transform the queries towards contextual information: Thus[66],

$$\text{Attention}(Q, K, V) = \text{softmax} \left( \frac{QK^T}{\sqrt{d}} \right) V \quad (\text{A5})$$

or more explicitly,

$$\text{Attention}(Q, K, V) = \sum_j \frac{\exp\{Q_i \cdot K_j / \sqrt{d}\}}{\sum_k \exp\{Q_i \cdot K_k / \sqrt{d}\}} V_{j,l} \quad (\text{A6})$$

where the elements  $\{V_{j,l}\}$  provide the contextual meaning of the  $j$ -th *key* vector. Thus, in some sense, Eqs. (A6) and (A2) carry out an importance-value projection where

$$\text{Importance} \equiv \left[ \text{softmax} \left( \frac{QK^T}{\sqrt{d}} \right) \right]_{i,j} \leftrightarrow \mathcal{M}_{\alpha_r, r}^{\mathcal{R}} \quad (\text{A7})$$

and

$$\text{Intrinsic Value} \equiv V_{j,l} \leftrightarrow \Delta E_{\alpha_r, r}(\bar{\mathbf{x}}) \quad (\text{A8})$$

together in the context of language provide context, and in the case of molecular potential energy surfaces, stability of a certain configuration. This connection can be made even more explicit by rewriting attention in bra-ket notation. In the absence of the softmax function, this map essentially writes the *query* vectors in the bi-orthogonal  $|K\rangle\langle V|$  basis and thus, in the absence of softmax,

$$\text{Attention}(Q, K, V) = \sum_K \langle Q|K\rangle \langle V| \quad (\text{A9})$$

and in the presence of softmax

$$\text{Attention}(Q, K, V) = \sum_K f(\langle Q|K\rangle) \langle V| \quad (\text{A10})$$

Thus the projections,  $\langle Q|K\rangle$  or  $f(\langle Q|K\rangle)$  act in an analogous fashion as the projections  $\mathcal{M}_{\alpha_r, r}$  in Eq. (S3) in SI.

However, even though it appears that these two problems may have a similar overarching strategy, the inherent differences between languages and molecules introduce challenges during different stages of the solution process. For molecules, constructing the graph is straightforward, and the weights can be calculated with well-defined inclusion and exclusion relationships. In contrast for language, the relationship between words is more complicated and abstract. Their relationship depends not only on their relative position in sentences but also on their meaning, coherence, and logical reasoning connections. Therefore, the attention is computed and optimized to understand the whole sentence through multiple layers of transformer architectures.

On the other hand, the primary challenge for molecules lies in obtaining accurate fragment-level information, specifically the fragment energies. Unlike words in language processing, which benefit from clear contextual information available from large and easily available language datasets for training, fragment energy modeling requires extensive and computationally expensive post-Hartree Fock calculations to generate training data. Thus, the neural network models used for fragment energy embedding often have limited accuracy and generalizability. For example, as we demonstrate in this paper, models trained on fragments from solvated zundel cannot be directly applied to the same sets of fragments from the protonated 21-water clusters. This limitation motivates the development of our systematic approach to incrementally expand the training space for fragment energy modeling.

- 
- [1] Murrell, J.; Carter, S.; Farantos, S.; Huxley, P.; Varandas, A. *Molecular Potential Energy Functions*; Wiley, New York, 1984.
  - [2] Braams, B. J.; Bowman, J. M. Permutationally invariant potential energy surfaces in high dimensionality. *Int. Revs. Phys. Chem.* **2009**, *28*, 577.
  - [3] Xie, Z.; Bowman, J. M. Permutationally Invariant Polynomial Basis for Molecular Energy Surface Fitting Via Monomial Symmetrization. *J. Chem. Theory and Comput.* **2010**, *6*, 26.
  - [4] Aliş, Ö. F.; Rabitz, H. Efficient implementation of high dimensional model representations. *J. Math. Chem.* **2001**, *29*, 127–142.
  - [5] Jäckle, A.; Meyer, H.-D. Product representation of potential energy surfaces. *J. Chem. Phys.* **1996**, *104*, 7974–7984.
  - [6] Peláez, D.; Meyer, H.-D. The multigrid POTFIT (MGPF) method: Grid representations of potentials for quantum dynamics of large systems. *J. Chem. Phys.* **2013**, *138*, 014108.
  - [7] Leclerc, A.; Carrington, T. Calculating vibrational spectra with sum of product basis functions without storing full-dimensional vectors or matrices. *The Journal of Chemical Physics* **2014**, *140*, 174111.
  - [8] Qu, C.; Conte, R.; Houston, P. L.; Bowman, J. M. Full-dimensional potential energy surface for acetylacetone and tunneling splittings. *Phys. Chem. Chem. Phys.* **2021**, *23*, 7758–7767.
  - [9] Grossmann, W.; Eilermann, S.; Rensmeyer, T.; Liebert, A.; Hohmann, M.; Wittke, C.; Niggemann, O. Position Paper on Materials Design – A Modern Approach. 2023; <https://arxiv.org/abs/2312.10996>.
  - [10] Vasudevan, R.; Pilania, G.; Balachandran, P. V. Machine learning for materials design and discovery. *Journal of Applied Physics* **2021**, *129*, 070401.
  - [11] Axelrod, S.; Schwalbe-Koda, D.; Mohapatra, S.; Damewood, J.; Greenman, K. P.; Gómez-Bombarelli, R. Learning Matter: Materials Design with Machine Learning and Atomistic Simulations. *Accounts of Materials Research* **2022**, *3*, 343–357.
  - [12] Persson, K.; Hinuma, Y.; Meng, Y. S.; Van der Ven, A.; Ceder, G. Thermodynamic and Kinetic Properties of the Li-Graphite System from First-Principles Calculations. *Phys. Rev. B* **2010**, *82*, 125416.
  - [13] Flam-Shepherd, D.; Zhigalin, A.; Aspuru-Guzik, A. Scalable Fragment-Based 3D Molecular Design with Reinforcement Learning. 2022.
  - [14] Feynman, R. P. Simulating physics with computers. *International Journal of Theoretical Physics* **1982**, *21*, 467–488.
  - [15] Feynman, R. P.; Hey, J.; Allen, R. W. *Feynman Lectures on Computation*; Addison-Wesley Longman Publishing Co., Inc., 1998.
  - [16] Feynman, R. P.; Hibbs, A. R. *Quantum Mechanics and Path Integrals*; McGraw-Hill Book Company: New York, 1965.
  - [17] Meyer, H.-D.; Manthe, U.; Cederbaum, L. S. The multi-configurational time-dependent Hartree approach. *Chem. Phys. Lett.* **1990**, *165*, 73–78.
  - [18] Nielsen, M. A.; Chuang, I. L. *Quantum computation and quantum information*; Cambridge University Press, Cambridge, 2000.
  - [19] Rabitz, H.; Aliş, Ö. F. General foundations of high dimensional model representations. *J. Math. Chem.* **1999**, *25*, 197–233.
  - [20] Manzhos, S.; Carrington Jr, T. Using neural networks, optimized coordinates, and high-dimensional model representations to obtain a vinyl bromide potential surface. *J. Chem. Phys.* **2008**, *129*, 224104.
  - [21] Otto, F. Multi-layer Potfit: An accurate potential representation for efficient high-dimensional quantum dynamics. *J. Chem. Phys.* **2014**, *140*, 014106.
  - [22] Sumner, I.; Iyengar, S. S. Quantum Wavepacket *Ab Initio* Molecular Dynamics: An Approach for Computing Dynamically Averaged Vibrational Spectra Including Critical Nuclear Quantum Effects. *J. Phys. Chem. A* **2007**, *111*, 10313.
  - [23] DeGregorio, N.; Iyengar, S. S. Efficient and Adaptive Methods for Computing Accurate Potential Surfaces for Quantum Nuclear Effects: Applications to Hydrogen-Transfer Reactions. *J. Chem. Theory Comput.* **2018**, *14*, 30–47.
  - [24] Schran, C.; Briec, F.; Marx, D. Transferability of machine learning potentials: Protonated water neural network potential applied to the protonated water hexamer. *J. Chem. Phys.* **2021**, 154.
  - [25] Nguyen, T. T.; Szekely, E.; Imbalzano, G.; Behler, J.; Csanyi, G.; Ceriotti, M.; Goetz, A. W.; Paesani, F. Comparison of permutationally invariant polynomials, neural networks, and Gaussian approximation potentials in representing water interactions through many-body expansions. *J. Chem. Phys.* **2018**, 148.
  - [26] Schran, C.; Behler, J.; Marx, D. Automated Fitting of Neural Network Potentials at Coupled Cluster Accuracy: Protonated Water Clusters as Testing Ground. *J. Chem. Theory Comput.* **2020**, *16*, 88–99.
  - [27] Lu, D.; Behler, J.; Li, J. Accurate Global Potential Energy Surfaces for the H + CH<sub>3</sub>OH Reaction by Neural Network Fitting with Permutation Invariance. *J. Phys. Chem. A* **2020**, *124*, 5737–5745.
  - [28] Lu, D.; Qi, J.; Yang, M.; Behler, J.; Song, H.; Li, J. Mode specific dynamics in the H<sub>2</sub> + SH → H + H<sub>2</sub>S reaction. *Phys. Chem. Chem. Phys.* **2016**, *18*, 29113–29121.
  - [29] Li, J.; Song, K.; Behler, J. A critical comparison of neural network potentials for molecular reaction dynamics with exact permutation symmetry. *Phys. Chem. Chem. Phys.* **2019**, *21*, 9672–9682.
  - [30] Smith, J. S.; Nebgen, B. T.; Zubatyuk, R.; Lubbers, N.; Devereux, C.; Barros, K.; Tretyak, S.; Isayev, O.; Roitberg, A. E. Approaching coupled cluster accuracy with a general-purpose neural network potential through transfer learning. *Nat Commun* **2019**, *10*, 2903.
  - [31] Li, A.; Guo, H. A nine-dimensional ab initio global potential energy surface for the H<sub>2</sub>O<sup>+</sup> + H<sub>2</sub> → H<sub>3</sub>O<sup>+</sup> + H reaction. *J. Chem. Phys.* **2014**, *140*, 224313.
  - [32] Lu, F.; Cheng, L.; DiRisio, R. J.; Finney, J. M.; Boyer, M. A.; Moonkaen, P.; Sun, J.; Lee, S. J. R.; Deustua, J. E.; Miller, T. F., III; McCoy, A. B. Fast



- Near Ab Initio Potential Energy Surfaces Using Machine Learning. *J. Phys. Chem. A* **2022**, 126, 4013–4024.
- [33] Aldossary, A.; Campos-Gonzalez-Angulo, J. A.; Pablo-García, S.; Leong, S. X.; Rajaonson, E. M.; Thiede, L.; Tom, G.; Wang, A.; Avagliano, D.; Aspuru-Guzik, A. In Silico Chemical Experiments in the Age of AI: From Quantum Chemistry to Machine Learning and Back. *Advanced Materials* **2024**, 36, 2402369.
- [34] Behler, J.; Parrinello, M. Generalized neural-network representation of high-dimensional potential-energy surfaces. *Phys. Rev. Lett.* **2007**, 98.
- [35] Behler, J. Four Generations of High-Dimensional Neural Network Potentials. *Chem. Rev.* **2021**, 121, 10037–10072.
- [36] Fournier, J. A.; Wolke, C. T.; Johnson, M. A.; Odbadrakh, T. T.; Jordan, K. D.; Kathmann, S. M.; Xantheas, S. S. Snapshots of Proton Accommodation at a Microscopic Water Surface: Understanding the Vibrational Spectral Signatures of the Charge Defect in Cryogenically Cooled  $\text{H}(\text{H}_2\text{O})_n^+$  = 2–28 Clusters. *J. Phys. Chem. A* **2015**, 119, 37.
- [37] Shin, J.-W.; Hammer, N. I.; Diken, E. G.; Johnson, M. A.; Walters, R. S.; Jaeger, T. D.; Duncan, M. A.; Christie, R. A.; Jordan, K. D. Infrared Signature of Structures Associated with the  $\text{H}^+(\text{H}_2\text{O})_n$  ( $N = 6$  to 27) Clusters. *Science* **2004**, 304, 1137.
- [38] Iyengar, S. S.; Petersen, M. K.; Day, T. J. F.; Burnham, C. J.; Teige, V. E.; Voth, G. A. The Properties of Ion-Water Clusters. I. the Protonated 21-Water Cluster. *J. Chem. Phys.* **2005**, 123, 084309.
- [39] Iyengar, S. S. Further Analysis of the Dynamically Averaged Vibrational Spectrum for the “magic” Protonated 21-Water Cluster. *J. Chem. Phys.* **2007**, 126, 216101.
- [40] Hammer, N. I.; Diken, E. G.; Roscioli, J. R.; Johnson, M. A.; Myshakin, E. M.; Jordan, K. D.; McCoy, A. B.; Huang, X.; Bowman, J. M.; Carter, S. The Vibrational Predissociation Spectra of the  $\text{H}_5\text{O}_2^+ \cdot \text{RG}_n$  ( $\text{RG} = \text{Ar, Ne}$ ) clusters: Correlation of the solvent perturbations in the free OH and shared proton transitions of the Zundel ion. *J. Chem. Phys.* **2005**, 122, 244301.
- [41] Headrick, J. M.; Diken, E. G.; Walters, R. S.; Hammer, N. I.; Christie, R. A.; Cui, J.; Myshakin, E. M.; Duncan, M. A.; Johnson, M. A.; Jordan, K. Spectral Signatures of Hydrated Proton Vibrations in Water Clusters. *Science* **2005**, 308, 1765.
- [42] Dietrick, S. M.; Iyengar, S. S. Constructing Periodic Phase Space Orbits from Ab Initio Molecular Dynamics Trajectories to Analyze Vibrational Spectra: Case Study of the Zundel ( $\text{H}_5\text{O}_2^+$ ) Cation. *J. Chem. Theory and Comp.* **2012**, 8, 4876.
- [43] Asmis, K. R.; Pivonka, N. L.; Santambrogio, G.; Brümmer, M.; Kaposta, C.; Neumark, D. M.; Wöste, L. Gas-Phase Infrared Spectrum of the Protonated Water Dimer. *Science* **2003**, 299, 1375.
- [44] Vendrell, O.; Gatti, F.; Meyer, H.-D. Dynamics and Infrared Spectroscopy of the Protonated Water Dimer. *Ang. Chem. Intl. Ed.* **2007**, 46, 6918.
- [45] Diken, E. G.; Headrick, J. M.; Roscioli, J. R.; Bopp, J. C.; Johnson, M. A.; McCoy, A. B. Fundamental Excitations of the Shared Proton in the  $\text{H}_3\text{O}_2^+$  and  $\text{H}_5\text{O}_2^+$  Complexes. *J. Phys. Chem. A* **2005**, 109, 1487.
- [46] Robertson, W. H.; Diken, E. G.; Price, E. A.; Shin, J.-W.; Johnson, M. A. Spectroscopic Determination of the OH<sup>-</sup> Solvation Shell in the  $\text{OH}^-(\text{H}_2\text{O})_n$  Clusters. *Science* **2003**, 299, 1367.
- [47] Li, J.; Iyengar, S. S. Ab initio Molecular Dynamics using Recursive, Spatially Separated, Overlapping Model Subsystems Mixed Within an ONIOM Based Fragmentation Energy Extrapolation Technique. *J. Chem. Theory Comput.* **2015**, 11, 3978–3991.
- [48] Li, J.; Haycraft, C.; Iyengar, S. S. Hybrid, Extended Lagrangian – Born-Oppenheimer *Ab Initio* Molecular Dynamics using Fragment-Based Electronic Structure. *J. Chem. Theory Comput.* **2016**, 12, 2493.
- [49] Haycraft, C.; Li, J.; Iyengar, S. S. Efficient, “On-the-fly” Born–Oppenheimer and Car–Parrinello–type Dynamics with coupled cluster accuracy through Fragment Based Electronic Structure. *J. Chem. Theory Comput.* **2017**, 13, 21887.
- [50] Ricard, T. C.; Haycraft, C.; Iyengar, S. S. Adaptive, geometric networks for efficient coarse-grained *ab initio* molecular dynamics with post-Hartree-Fock accuracy. *J. Chem. Theory Comput.* **2018**, 14, 2852.
- [51] Ricard, T. C.; Iyengar, S. S. Efficiently capturing weak interactions in *ab initio* molecular dynamics through “on-the-fly” basis set extrapolation. *J. Chem. Theory Comput.* **2018**, 14, 5535.
- [52] Kumar, A.; Iyengar, S. S. Fragment-based electronic structure for potential energy surfaces using a superposition of fragmentation topologies. *J. Chem. Theory Comput.* **2019**, 15, 5769.
- [53] Ricard, T. C.; Iyengar, S. S. An efficient and accurate approach to estimate hybrid functional and large basis set contributions to condensed phase systems and molecule-surface interactions. *J. Chem. Theory Comput.* **2020**, 16, 4790.
- [54] Ricard, T. C.; Kumar, A.; Iyengar, S. S. Embedded, graph-theoretically defined many-body approximations for wavefunction-in-DFT and DFT-in-DFT: Applications to gas- and condensed-phase *ab initio* molecular dynamics, and potential surfaces for quantum nuclear effects. *Int. J. Quantum Chem.* **2020**, 120, e26244.
- [55] Ricard, T. C.; Zhu, X.; Iyengar, S. S. Capturing weak interactions in surface adsorbate systems at coupled cluster accuracy: a graph-theoretic molecular fragmentation approach improved through machine learning. *J. Chem. Theory Comput.* **2023**, 19, 8541.
- [56] Kumar, A.; DeGregorio, N.; Iyengar, S. S. Graph-Theory-Based Molecular Fragmentation for Efficient and Accurate Potential Surface Calculations in Multiple Dimensions. *J. Chem. Theory Comput.* **2021**, 17, 6671–6690.
- [57] Zhang, J. H.; Ricard, T. C.; Haycraft, C.; Iyengar, S. S. Weighted-Graph-Theoretic Methods for Many-Body Corrections within ONIOM: Smooth AIMD and the Role of High-Order Many-Body Terms. *J. Chem. Theory Comput.* **2021**, 17, 2672–2690.
- [58] Zhu, X.; Iyengar, S. S. Graph Theoretic Molecular Fragmentation for Multidimensional Potential Energy Surfaces Yield an Adaptive and General Transfer Machine Learning Protocol. *J. Chem. Theory Comput.* **2022**, 18,

- 5125–5144.
- [59] Zhang, J. H.; Iyengar, S. S. Graph- $|Q\rangle\langle C|$ : A Graph-based Quantum-classical algorithm for efficient electronic structure on hybrid quantum/classical hardware systems: Improved quantum circuit depth performance. *J. Chem. Theory Comput.* **2022**, 18, 2885.
- [60] Kumar, A.; DeGregorio, N.; Ricard, T.; Iyengar, S. S. Graph-Theoretic Molecular Fragmentation for Potential Surfaces Leads Naturally to a Tensor Network Form and Allows Accurate and Efficient Quantum Nuclear Dynamics. *J. Chem. Theory Comput.* **2022**, 18, 7243.
- [61] Iyengar, S. S.; Saha, D.; Dwivedi, A.; Lopez-Ruiz, M. A.; Kumar, A.; Zhang, J. H.; Ricard, T. C.; Richerme, P.; Sabry, A. Quantum Algorithms for the Study of Electronic Structure and Molecular Dynamics: Novel Computational Protocols. In *Comprehensive Computational Chemistry*; Elsevier, 2023.
- [62] Iyengar, S. S.; Zhang, J. H.; Saha, D.; Ricard, T. C. Graph- $|Q\rangle\langle C|$ : A Quantum Algorithm with Reduced Quantum Circuit Depth for Electronic Structure. *J. Phys. Chem. A* **2023**, 127, 9334.
- [63] Iyengar, S. S.; Ricard, T. C.; Zhu, X. A reformulation of all ONIOM-type molecular fragmentation approaches using graph theory-based projection operators: Applications to dynamics, molecular potential surfaces, and machine learning and quantum computing. *J. Phys. Chem. A* **2024**, 128, 466.
- [64] Zhang, W.; Itoh, K.; Tanida, J.; Ichioka, Y. Parallel distributed processing model with local space-invariant interconnections and its optical architecture. *Appl. Opt.* **1990**, 29, 4790–4797.
- [65] Duvenaud, D. K.; Maclaurin, D.; Iparraguirre, J.; Bombarell, R.; Hirzel, T.; Aspuru-Guzik, A.; Adams, R. P. Convolutional networks on graphs for learning molecular fingerprints. *Advances in neural information processing systems*. 2015; pp 2224–2232.
- [66] Vaswani, A.; Shazeer, N.; Parmar, N.; Uszkoreit, J.; Jones, L.; Gomez, A. N.; Kaiser, L. u.; Polosukhin, I. Attention is All you Need. *Advances in Neural Information Processing Systems*. Guyon, I., Luxburg, U. V., Bengio, S., Wallach, H., Fergus, R., Vishwanathan, S., Garnett, R., Eds.; Curran Associates, Inc., 2017; Vol. 30.

## SUPPORTING INFORMATION

### A large language model-type architecture for high-dimensional molecular potential energy surfaces

Xiao Zhu, Srinivasan S. Iyengar,<sup>1</sup>

<sup>1</sup>*Department of Chemistry, Department of Physics,  
and the Indiana University Quantum Science and Engineering Center (IU-QSEC),  
Indiana University, 800 E. Kirkwood Ave, Bloomington, IN-47405*

(Dated: December 6, 2024)

This Supporting Information document is organized as follows. In section S1, we analyze and estimate the complexity of obtaining sufficient training samples for accurate electronic potential energy surfaces. In section S2, we briefly outline our graph theory-based neural network procedure. Further details can be found in references 1 and 2. We also introduce a systematic procedure for constructing permutation invariant interatomic distances that are used as descriptor for fragments within our ML paradigm. In section ??, we present a comparative analysis between computing molecular potential energy surfaces and natural languages. In Section S3, we analyze the differences between fragments obtained from different systems and discuss how an existing learning model can be transformed to provide accurate models for more complex systems. In Section S4 we outline our transformer learning platform. The k-means sampling method and the specific neural network model setting are introduced in Section S5. Section S6 illustrates how fragment accuracy is improved through incremental learning. Section S7 summarizes the computational costs associated with the methods discussed here.

#### S1. THE CHALLENGE OF OBTAIN TRAINING DATA FOR POST-HARTREE-FOCK POTENTIAL SURFACES AND THE ASSOCIATED NEURAL NETWORK COMPLEXITY

The authors in Refs. 1–8 have constructed potential energy surfaces for complex systems using multiple training set sizes at the couple-cluster level of theories. Although the number of training samples used is very different in each of the studies, for example the blue dots in Figure S1, the data generally indicates that larger systems sometimes require potentially exponentially more training samples due to higher dimensionality, and a theoretical estimate of the number of training samples needed from the perspective of complexity or the number of weights in an associated neural network model is provided using the blue trace in Figure S1. Since poten-

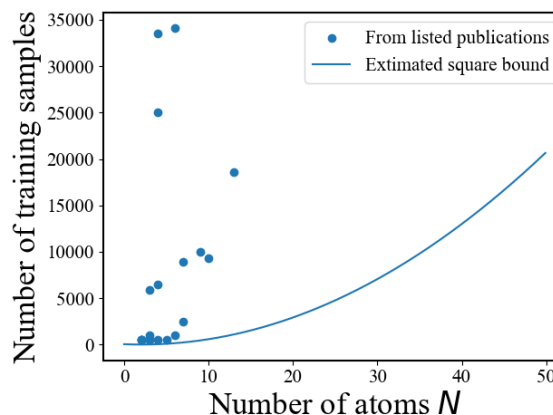


FIG. S1. The number of training samples used in Refs. [3–7] for potential energy surface construction at coupled cluster accuracy is shown with blue dots. The red trace shows an estimated lower bound for network complexity.

tial energy surfaces have dimensionality of  $3N - 6$  for  $N$  atoms, the number of features needed to describe this surface for a neural network should be at least of the order of  $3N - 6$ , implying that at least the same number of nodes is required in the input and hidden layers of a suitable neural network. Thus, the total number of weights connecting neighboring layers in a neural network may scale as  $O(N^2) \equiv (3N - 6)^2$ . To optimize these weights, an equivalent number of training samples may sometimes be necessary. In Figure S1, we show the number of training samples used in Refs. 3–7 along with the quadratic estimate of the required number of training samples based on the above discussion. In practice, the scaling of training data needed appears to be far more than that shown from arguments purely based on network complexity. Additionally, Figure S1 also shows the extent to which, the training complexity constrains the size of the systems that can be studied, especially when coupled cluster accuracy is needed. To date, the largest systems studied using machine learning that de-

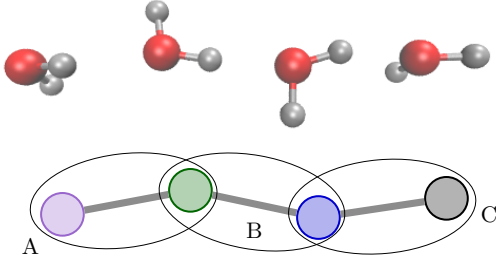


FIG. S2. Illustration of sets and graphs described in Section S2. The water wire on top is represented as a graph, with nodes being individual water molecules, and the graph also defines the sets  $A$ ,  $B$  and  $C$ .

livers coupled cluster accuracy potential surfaces are of the order of 10s of degrees of freedom. In this paper, for the first time, we push that envelope to 100s of degrees of freedom.

## S2. GRAPH-THEORY-BASED NEURAL NETWORK PROTOCOLS

We summarize here our protocol to divide a large system into individual, overlapping fragments, namely,  $\{A, B, C, \dots\}$ . Figure S2 illustrates how this process is conducted. The corresponding electronic Hilbert space that defines the full molecule may be, for simplicity, represented in the coordinate representation,  $\{|x\rangle\}$ . In general, we may resolve the identity, using individual projectors,  $\{\mathcal{P}_A, \mathcal{P}_B, \dots\}$ , along with the set-theoretic inclusion-exclusion principle[9] as

$$\begin{aligned} \mathbf{I} = & \mathcal{P}_A + \mathcal{P}_B + \mathcal{P}_C + \dots \\ & - \mathcal{P}_{A \cap B} - \mathcal{P}_{A \cap C} - \mathcal{P}_{B \cap C} - \dots \\ & + \mathcal{P}_{A \cap B \cap C} + \dots \\ & \dots \end{aligned} \quad (\text{S1})$$

where

$$\mathcal{P}_A = \int_A |x\rangle\langle x|. \quad (\text{S2})$$

In refs. [1, 8, 10, 11], we have shown that a graph theoretic representation of molecular fragments provides a similar, but more robust, formalism to divide the molecular space using nodes, edges, faces, and higher rank simplexes[12–14] that constitute a graph. The set of rank- $r$  simplexes,  $\mathbf{V}_r$  where each unique element or fragment within the set is labeled as  $\alpha_r$  resemble the non-overlapping regions  $\{A', B', C', \dots\}$  and their unions  $\{A' \cup B', B' \cup C', A' \cup C', \dots\}$ ,  $\{A' \cup B' \cup C', \dots\}$  and so on, and thus yields an alternative way to represent the molecule’s electronic Hilbert space through a set of

projection operators  $\mathcal{P}_{\alpha_r, r}$  to obtain[1, 8, 10, 11]

$$\mathbf{I} = \sum_r \sum_{\alpha_r \in \mathbf{V}_r} \mathcal{M}_{\alpha_r, r} \mathcal{P}_{\alpha_r, r}. \quad (\text{S3})$$

Here, the quantity,

$$\mathcal{M}_{\alpha_r, r} = \sum_{m \geq r} (-1)^{m+r} p_{\alpha_r}^{r, m}. \quad (\text{S4})$$

represents the total number of times the simplex  $\alpha_r \in \mathbf{V}_r$  appears in all simplexes with rank greater than  $r$ . Thus,  $\mathcal{M}_{\alpha_r, r}$  is an over-counting correction and  $p_{\alpha_r}^{r, m}$  is the number of times the  $\alpha_r^{\text{th}}$  rank- $r$  simplex is included within all rank- $m$  simplexes, for  $m \geq r$ . When the operator in Eq. (S3) is applied to a molecular system it will decompose the system into fragments represented using nodes (local, connected or interacting groups of atoms), edges (node-node interactions and this may include connected, bonded, or disconnected, and hence through space interactions), faces (three-node interactions), tetrahedrons (four-node interactions), etc, and produce an energy expression[1, 2, 10, 15–25],

$$E_{\text{graph, MBE}}^{\text{target}}(\bar{\mathbf{x}}) = \sum_{r=0}^{\mathcal{R}} \sum_{\alpha \in \mathbf{V}_r} \mathcal{M}_{\alpha_r, r}^{\mathcal{R}} E_{\alpha_r, r}^{\text{target}}(\bar{\mathbf{x}}) \quad (\text{S5})$$

and “target” here is some target level of electronic structure theory, such as CCSD etc, which would otherwise scale as  $\mathcal{O}(N^{6 \dots 7})$ . The application of Eq. (S3) onto the full system hence yields a set of fragment energies  $\{E_{\alpha_r, r}^{\text{target}}(\bar{\mathbf{x}})\}$  that then provide an approximation to the total energy as per Eq. (S5). The quantity  $\bar{\mathbf{x}}$  represents a given molecular geometry and the quantity  $\mathcal{R}$  is the highest rank simplex included within the approximation. Connections between Eq. (S5) and the commonly used many-body expansions have been discussed in Refs. [18, 19, 24].

However, it has been shown in Refs. [21, 24] that such an approximation converges slower with the maximum truncation order  $\mathcal{R}$  above as compared to one where Eq. (S5) is included within an ONIOM-like[26] formalism to obtain

$$\begin{aligned} E^{\text{target}}(\bar{\mathbf{x}}) = & E^{\text{Ref.}}(\bar{\mathbf{x}}) + \\ & \sum_{r=0}^{\mathcal{R}} \sum_{\alpha_r \in \mathbf{V}_r} \mathcal{M}_{\alpha_r, r}^{\mathcal{R}} \Delta E_{\alpha_r, r}(\bar{\mathbf{x}}) \end{aligned} \quad (\text{S6})$$

which is Eq. (2) in the main paper. Here

$$\Delta E_{\alpha_r, r}(\bar{\mathbf{x}}) = E_{\alpha_r, r}^{\text{target}}(\bar{\mathbf{x}}) - E_{\alpha_r, r}^{\text{Ref.}}(\bar{\mathbf{x}}) \quad (\text{S7})$$

where “Ref.” is some reference electronic structure level such as DFT. In Eq.S6, a high-level energy correction  $\Delta E_{\alpha_r, r}$  for each fragment or simplex in  $\mathbf{V}_r$  is added to a reference energy, such as DFT. This energy expression in Eq. S6 has been demonstrated by performing

accurate AIMD studies at post Hartree-Fock accuracy with DFT cost, accurate large basis AIMD trajectories for gas phase and condensed phase systems[2, 15–25], and has been used to obtain new quantum computing algorithms[10], machine learning protocols[1] and molecular potential energy surfaces[20, 23, 25].

However, as the complexity and size of the system grow, we find that this approach also becomes expensive by needing post-Hartree-Fock energies and gradients for larger and larger clusters obtained from higher rank objects discussed above. That is  $\{E_{\alpha_r,r}^{target}(\bar{\mathbf{x}})\}$  may be needed for larger and larger values of  $r$ . Furthermore, the number of fragments produced could also grow rapidly as the system size grows since higher rank objects can be formed by all possible combinations of nodes within a distance cutoff. In Refs. [1, 2], we provided machine learning approximations for the larger clusters, so as to scale down the cost of obtaining potential surfaces for large gas-phase and condensed-phase problems. In other words, we use neural network predictions for  $\Delta E_{\alpha_r,r}^{ML}(\bar{\mathbf{x}})$  to replace the larger rank  $\Delta E_{\alpha_r,r}$  values in Eq. S7. This is achieved by first assuming the existence of some neural network learning model,  $\mathcal{Q}$ , which provides the energy of the system at the “target” post-Hartree Fock level,

$$\bar{x} \xrightarrow{\mathcal{Q}} E^{target}(\bar{x}) \quad (\text{S8})$$

Such a neural network,  $\mathcal{Q}$  may be visually represented, for example, by the network in Figure 1 in the main paper. We may then simplify  $\mathcal{Q}$  using Eq. S3 to obtain

$$\begin{aligned} \mathbf{I} \mathcal{Q} &\approx \left[ \sum_{r=0}^{\mathcal{R}} (-1)^r \sum_{\alpha_r \in \mathbf{V}_r} \mathcal{M}_{\alpha_r,r} \mathcal{P}_{\alpha_r,r} \right] \mathcal{Q} \\ &= \sum_{r=0}^{\mathcal{R}} (-1)^r \sum_{\alpha_r \in \mathbf{V}_r} \mathcal{M}_{\alpha_r,r} \mathcal{Q}_{\alpha_r,r}. \end{aligned} \quad (\text{S9})$$

The full system neural network mapping  $\mathcal{Q}$  now has been decomposed into a family of much smaller neural networks  $\{\mathcal{Q}_{\alpha_r,r}\}$  that depends only on the corresponding fragment geometry. Consequently, the cost of preparing training samples from fragments becomes much easier, and the complexity of neural networks is also largely reduced.[1, 2, 8] The corresponding energy expression, in Eq. (S6) then becomes

$$\begin{aligned} E_{ML}^{target}(\bar{\mathbf{x}}) &= E^{Ref}(\bar{\mathbf{x}}) + \sum_{r=0}^{\mathcal{R}} \sum_{\alpha_r \in \mathbf{V}_r} \mathcal{M}_{\alpha_r,r}^{\mathcal{R}} \Delta E_{\alpha_r,r}^{ML}(\bar{\mathbf{x}}) \\ &= E^{Ref}(\bar{\mathbf{x}}) + \sum_{r=0}^{\mathcal{R}} \Delta E_r^{ML}(\bar{\mathbf{x}}) \end{aligned} \quad (\text{S10})$$

Thus the ML error is

$$\begin{aligned} E_{ML}^{target}(\bar{\mathbf{x}}) - E^{target}(\bar{\mathbf{x}}) &= \sum_{r=0}^{\mathcal{R}} \sum_{\alpha_r \in \mathbf{V}_r} \mathcal{M}_{\alpha_r,r}^{\mathcal{R}} (\Delta E_{\alpha_r,r}^{ML}(\bar{\mathbf{x}}) - \Delta E_{\alpha_r,r}(\bar{\mathbf{x}})) \end{aligned} \quad (\text{S11})$$

and the quantity,

$$\omega_{r,\mathcal{R}} = \frac{\sum_{\alpha_r \in \mathbf{V}_r} |\mathcal{M}_{\alpha_r,r}^{\mathcal{R}}|}{\sum_{r'=0}^{\mathcal{R}} \sum_{\alpha_r \in \mathbf{V}_{r'}} |\mathcal{M}_{\alpha_r,r'}^{\mathcal{R}}|} \quad (\text{S12})$$

is the relative significance of all rank- $r$  fragments in Eqs. (S6) and (S10). Alternately, a specific kind of fragment of rank- $r$ ,  $f_r \subseteq \mathbf{V}_r$ , may have significance given by

$$\omega_{f_r,\mathcal{R}} = \frac{\sum_{\alpha_r \in f_r} |\mathcal{M}_{\alpha_r,r}^{\mathcal{R}}|}{\sum_{r'=0}^{\mathcal{R}} \sum_{\alpha_r \in \mathbf{V}_{r'}} |\mathcal{M}_{\alpha_r,r'}^{\mathcal{R}}|} \quad (\text{S13})$$

The simplification afforded by this approximation may be seen from the visual depictions provided in the main paper in Figures 1-3, where we have shown how the neural networks for  $\{\Delta E_{\alpha_r,r}^{ML}(\bar{\mathbf{x}})\}$  can be used to construct approximations to  $\{\Delta E_r^{ML}(\bar{\mathbf{x}})\}$  and finally  $E_{ML}^{target}(\bar{\mathbf{x}})$ . In Figure 2 in the main paper, we show the independent neural networks for each node that contribute to  $\{\Delta E_{\alpha_r,r=0}^{ML}(\bar{\mathbf{x}})\}$  terms in Eq. (S10), which combined with the respective multiplicities,  $\{\mathcal{M}_{\alpha_r,r}^{\mathcal{R}}\}$  yield  $\{\Delta E_{r=0}^{ML}(\bar{\mathbf{x}})\}$ . Similarly, in Figure 3 we show the independent neural networks for each edge and these two figures visually convey the reduced complexity of obtaining these fragment neural networks as can be seen by comparison with Figure 1.

#### A. K-means clustering approach for reduction in fragment training set

The application of Eq. (S10) has been demonstrated for gas-phase[1] and condensed phase studies[2]. A critical part of this analysis involves a reduction in the amount of training data needed, since this aspect critically influences the application of such algorithms as discussed above. The approach used in Ref. [1] to arrive at a minimal set of training data is as follows. We compute AIMD trajectories at some reference level which may be of lower complexity or similar to the level depicted as “Ref.” above. Then, this reference data is tessellated using a k-means clustering algorithm[27] and the resultant data is used as the training set to construct neural network approximations to  $\{\Delta E_{\alpha_r,r}^{ML}(\bar{\mathbf{x}})\}$ . Using this idea we have shown that *only* 10% of AIMD data is needed to achieve milli-Hartree accuracy (chemical accuracy) for energies of configurations obtained in the entire trajectory.

Here, we also show that this approach can be generalized to grow more complex neural networks that are applicable to even larger systems than systems for which these neural networks were designed (that is the ones used in computing the AIMD trajectories mentioned above). For example, in the next section, we will show how cluster neural networks that were originally defined to obtain accurate potential surfaces for the solvated zundel system, can now be generalized to obtain results for the protonated 21 water cluster. Thus, in a sense, this paper provides the first milli-Hartree level neural network description of larger water clusters.

### B. A consistent frame of reference for describing fragments (descriptors)

A key question that we address in this publication is whether the neural network models created for the fragments within a smaller system, such as the solvated Zundel system, can be transferred to a larger system, such as a larger protonated 21-water cluster system in our case. In this section we raise the issues that arise from such a goal and then provide numerical solutions towards incremental learning.

We first intend to introduce a consistent framework of description of fragment geometries that arise from different molecular systems. Such a descriptor should allow for translational, rotational, and permutational invariance within the fragments, so that chemically identical fragments derived from different systems, or such fragments derived from different physical regions of the same system, have the same consistent mathematical description and thus can be compared with each other.

We begin with the inter-atomic distance matrix of fragments as descriptors but then recognize that the ordering of atoms between fragments may not be chemically consistent. For example, let us consider a water-wire fragment  $((\text{H}_2\text{O})_n)$  fragment which is found in multiple chemical systems and has a critical role in proton transfer in water clusters and in condensed phase systems. Hence a fragment of this kind can be found in most water cluster systems. An example of such a system can be found in Figure S3. This specific system contains eight protons, but all eight protons do not have the same chemical environment and properties. While five protons are on the periphery, three protons are shared between two oxygen atoms. Additionally, the shared protons themselves have different secondary environments. For larger water clusters these differences become further complicated where our chemical description of the cluster must maintain a distinction between the shared protons on the outer layers of the cluster and those on the inner layers. To arrive at a consistent notation that retains the chemical meaning of each atom, we use the following steps

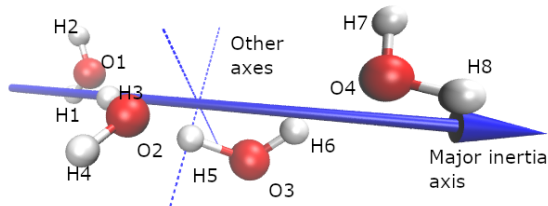


FIG. S3. An illustration of the moment of inertia frame of reference and the corresponding atom ordering for a four water wire fragment. The major axis is the mass moment of inertia axis with the smallest absolute mass moment of inertia. The dash lines represent the two other inertia axes.

1. We first rotate the fragment geometry coordinates into center of mass coordinates and mass moment of inertia frame of reference. In Figure S3, the large blue axis refers to the axis of the major moment of inertia, that is smallest inertia value.
2. Following this the atoms are ordered in increasing order of atomic weights, and then
  - (a) increasing order of coordinate projection along the major moment of inertia axis.
  - (b) For cases where the major axis projected value is identical, the second major axis projection value is used to resolve the order of atoms.
3. We then arrive at an ordered list of atoms for any given fragment that consistently represents the chemical environment that the specific atom resides within.
4. After permuting all atoms based on the relative positions along the fragment moment of inertia axis, the distance matrix is computed and reshaped into a vector to define the fragment descriptor.

### S3. THE CHALLENGE OF TRANSFERRING FRAGMENT NEURAL NETWORKS ACROSS MOLECULAR SYSTEMS

Our goal in this section is to lay the ground work to transfer the neural networks computed from a solvated zundel database to the larger protonated 21 water cluster database. However, the range of fragment structures that significantly contribute to the solvated zundel system could be very different from those that contribute to protonated 21 water cluster system. If that were the case, it would present a significant challenge. To gauge the extent to which the range of structures defers between the two libraries, we first examine the differences in distributions of fragment geometries as they appear in a solvated zundel system with that obtained for a

larger protonated 21 water cluster system. We generate two ab initio molecular dynamics trajectories to generate the corresponding library of structures – one for a solvated zundel including 9326 geometry frames, and one for a protonated 21 water cluster including 28294 frames. These AIMD geometries are obtained using the graph theoretic fragmentation energy expressions (Eq. (S6)) along with gradients as discussed in Refs. 2, 15–25). The quantity  $E^{Ref}$  is chosen as DFT, and the *target* level is CCSD.[17] We considered at most rank 3 simplexes ( $\mathcal{R} = 3$  in Eq. (S6), and hence four-body interactions) in both trajectories with maximum oxygen-oxygen distance (which defines the maximum edge length to define the graph) values set at 7.5Å for the solvated zundel and 4.5Å for the protonated 21 water cluster respectively[24]. Additionally, the hydrogen-oxygen distance cutoff value is set to be 1.4Å and defines the chemical bonding environment used to obtain the graphs and fragments. These choices are based on our previous studies[15–17, 24]. The number of fragments of each kind obtained during both trajectories is summarized in Table S1.

Fragment	$(H_2O)_6H^+$ data <sup>a</sup>		$(H_2O)_{21}H^+$ data <sup>b</sup>
	Full data	Training dataset size <sup>c</sup>	Target data
$H_2O$	38910	3891	559877
$H_3O^+$	17046	1704	34297
$H_4O_2$	62380	6238	1356707
$H_5O_2^+$	77510	7751	190727
$H_6O_2^{++d}$	0	0	99
$H_6O_3$	46940	4694	1014960
$H_7O_3^+$	139580	13958	257260
$H_8O_3^{++d}$	0	0	256
$H_8O_4$	15750	1575	253889
$H_9O_4^+$	124140	12414	108123
$H_{10}O_4^{++d}$	0	0	71

<sup>a</sup> Number of fragments from the  $(H_2O)_6H^+$  trajectory.

<sup>b</sup> Number of fragments from the  $(H_2O)_{21}H^+$  trajectory.

<sup>c</sup> Neural network training data size. These data points are obtained from a multi-dimensional k-means clustering algorithm[1, 27] of the Full  $(H_2O)_6H^+$  data and represent 10% of the data set.

<sup>d</sup> Very low probability doubly protonated fragments found in the larger 21-water cluster but not in solvated Zundel.

TABLE S1. Number of fragments in the solvated zundel library, the corresponding number of data points in a training library and the library size for the protonated 21 water cluster system used for testing predictions.

We begin with the neural networks previously developed[1] for the fragments in Table S1 using the solvated Zundel data. To develop these neural networks, we generate training sets using the k-means clustering[1, 27] method. We perform k-means clustering[27] calculations on the database of fragment structures obtained from solvated Zundel AIMD trajectory to create a representa-

tive training set for the fragments in the solvated Zundel system. Using k-means we divide or tessellate the data space for each fragment type in Table S1 into regions, and these regions are called clusters. Each cluster is represented by a centroid that is computed as the arithmetic mean of all data points in that specific cluster. This primitive training set (that is the set of centroids obtained from k-means) is chosen to be 10% in size (as compared to the full data set for the solvated Zundel system in Table S1) and is used to construct neural networks and fragment energies needed in Eq. (S10). Examples of such neural networks are shown in Figures 2 and 3 in the main paper. These neural networks are used to then compute energy values for the data from the full trajectory for solvated Zundel as well as the 21-mer with fragment energy errors for the target level of the theory given in Table S2 and the distribution of errors for full system geometries for both systems being given in Figure S4. In Table S2, we also present the quantity  $\omega_{f_r, \mathcal{R}}$  in Eq. (S13), which gauges the significance of each fragment in the overall *target* energy. We already see that some of the larger sized fragments are more significant in the 21-water cluster than they were in the solvated Zundel system which could be expected to have an important role on the overall error.

Fragments	$(H_2O)_6H^+$		$(H_2O)_{21}H^+$	
	$\omega_{f_r, \mathcal{R}}$ <sup>a</sup>	MAE <sup>b</sup>	$\omega_{f_r, \mathcal{R}}$ <sup>c</sup>	MAE <sup>d</sup>
$H_2O$	0.13	0.00	0.14	0.00
$H_3O^+$	0.06	0.00	0.01	0.00
$H_4O_2$	0.16	0.01	0.30	0.06
$H_5O_2^+$	0.20	0.01	0.04	0.15
$H_6O_3$	0.08	0.01	0.28	0.31
$H_7O_3^+$	0.24	0.02	0.06	0.45
$H_8O_4$	0.01	0.04	0.12	0.59
$H_9O_4^+$	0.11	0.05	0.05	0.88

<sup>a</sup> For fragments found in the  $(H_2O)_6H^+$  AIMD trajectory at  $R = 3$  from Eq.S13.

<sup>b</sup> MAE for fragments found in the  $(H_2O)_6H^+$  AIMD trajectory.

<sup>c</sup> For fragments found in the  $(H_2O)_{21}H^+$  AIMD trajectory at  $R = 3$  from Eq.S13.

<sup>d</sup> MAE for fragments found in the  $(H_2O)_{21}H^+$  AIMD trajectory.

TABLE S2. Mean absolute error(MAE) in kcal/mol from initial models trained on 10% solvated zundel fragments (see Table S1) and predictions for both solvated zundel fragments and protonated 21 water cluster fragments.

As can be seen from Table S2 and Figure S4, for the 10% training, we can construct highly accurate models for solvated Zundel fragment energies and obtain full system potential energies with an MAE of 0.36 kcal/mol. Additionally, most of the structures are in the sub-kcal/mol range. However, when these same neural network models are used to evaluate the *target* energies for the structures in the larger protonated 21 water clusters, the full system error has raised to 5.32 kcal/mol, with a substantial population of structures with errors greater

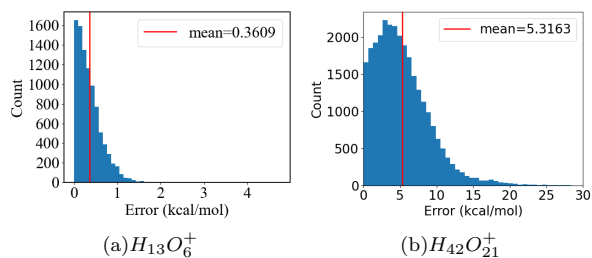


FIG. S4. The absolute error distribution (blue) and MAE (red) for solvated zundel (a) and protonated 21 water cluster (b) full system potential energies from Eq. S6 by using fragment energies with errors noted in Table S2. While computing the potential energy for the 21-water cluster, the energy corrections of doubly protonated fragments not shown in the solvated zundel are predicted as 0 kcal/mol. Because of this, there are 4 geometries predicted with around 120 kcal/mol error not shown in (b). Due to their low occurrence, these fragments do not affect our test for the transferability.

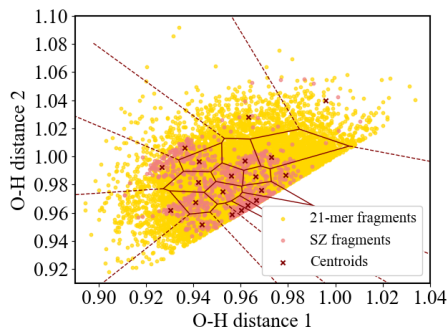


FIG. S5. Distribution of data for the water fragments, and corresponding centroids obtained from k-means. The centroids were derived from the solvated Zundel data (see Table S1). Note that all data lies above the line where the two  $O - H$  distances are equal, since “OH distance 1” is always the shorter distance. Clustering is conducted only on the two  $O - H$  distances for demonstration.

than 10kcal/mol. This is because the larger fragments, beginning with the protonated water dimer systems, contain geometries that are very different in the protonated 21-water cluster trajectory as compared to the solvated zundel trajectory. These differences in fragment structures are responsible for the larger errors in fragment energies in Table S2 and Figure S4 and as a consequence the full system error accumulates rapidly with fragment errors according to Eq. S10.

To quantify the extent to which the fragment structures differ between the two systems, we first gauge the distribution of data around the training set centroids. A simplified heuristic for such a data distribution is provided in Figure S5 for water fragments found within

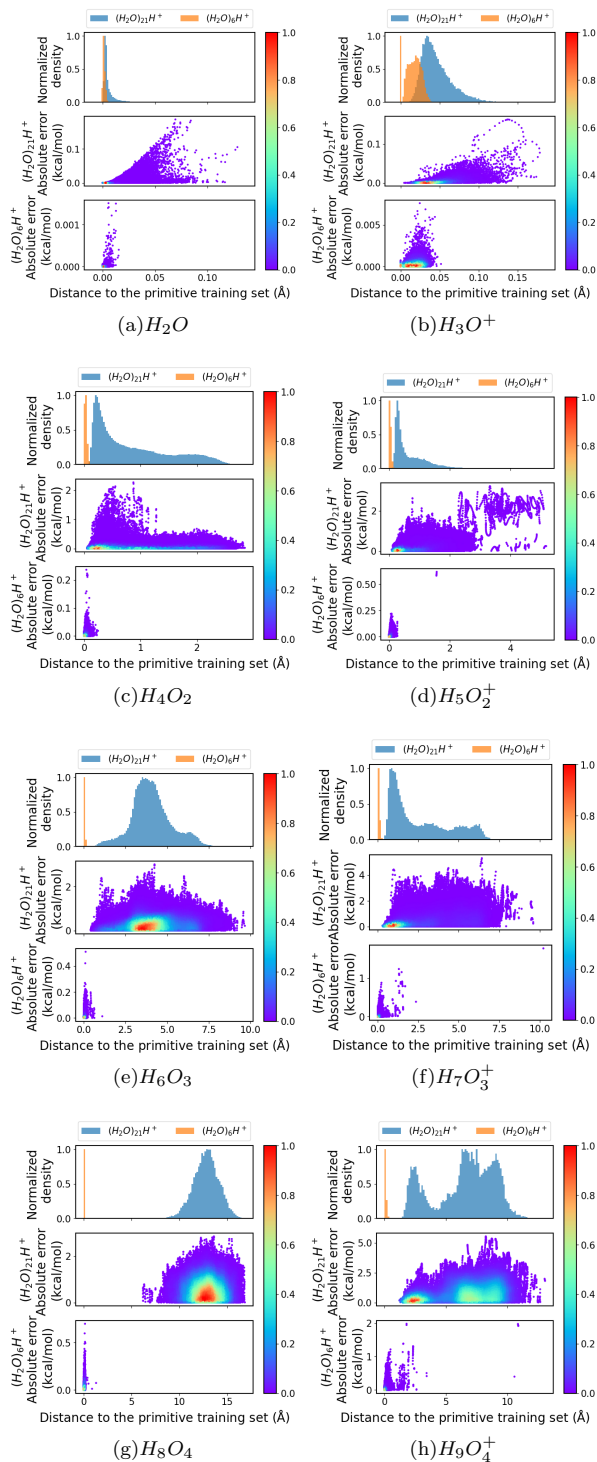


FIG. S6. Fragment data proximity from nearest training point (horizontal axis) and respective distributions (top panel). The absolute error is computed from the neural network predictions trained on solvated zundel fragments. Color bars represent relative density.



both the solvated Zundel as well as the 21-water cluster. Clearly, the data distribution is very different even for such a small fragment. To further probe this difference, we consider the Cartesian distance between the descriptor vector for the k-means centroids and the data points from the two systems, that is, in some sense the level of confidence for a given data point given its proximity to a training point. We then compute the distribution of these Cartesian distances from each fragment to their closest training geometries (obtained from the k-means centroid geometries) and these are shown along the horizontal axes in Figures S6. The distributions of distances for fragments from the two systems are displayed using two histograms in the top panels in Figure S6. From the top panels of each figure in Figure S6, a clear distinction between the distributions for the two systems begins to appear from  $H_4O_2$ , which coincides with the pattern of MAE differences in Table S2. As the size of the fragment increases, the difference in geometry distribution also increases as shown by the right-shifting peaks of blue histograms on the top panels of Figure S6.

In the middle and bottom panels of each figure of Figure S6 we present the error in *target* energy for 21-mer fragments and the error in CCSD energy for the solvated zundel fragments respectively, which results from the difference in the distribution of data noted above. From the scale of the vertical axes in the middle and bottom panels, the effect of this perturbation in distribution is already clear. This strongly indicates that for geometries with large distances to the primitive training set, the predictive accuracy is generally low. Therefore, an amended transferring process needs to be designed to expand the valid training set regions to build confidence in the accuracy of predictions for all geometries.

#### S4. A TRANSFORMER LEARNING PLATFORM TO REFINE THE FRAGMENT NEURAL NETWORKS TOWARDS THE *target*

We wish to expand the previously defined training set regions (see Figures S4, S5 and S6), using the portion of the 21-mer data that are not visited in solvated Zundel trajectory, and obtain a new family of neural networks that apply to both the solvated Zundel data and 21-mer geometries. As seen from Figures S5 and S6, the data space deviations becomes significantly large, as one moves from the solvated Zundel data to the 21-mer data. While this aspect may not be clear from Figure S5, the use of k-means to model the 21-mer data directly, will in general be (a) confounded by this potentially exponentially large data size, and (b) the resultant model will be heavily weighted by the larger 21-mer data and not be sufficiently representative of the solvated Zundel data.

To address these problems, we now introduce a systematic process to incrementally expand the domain of

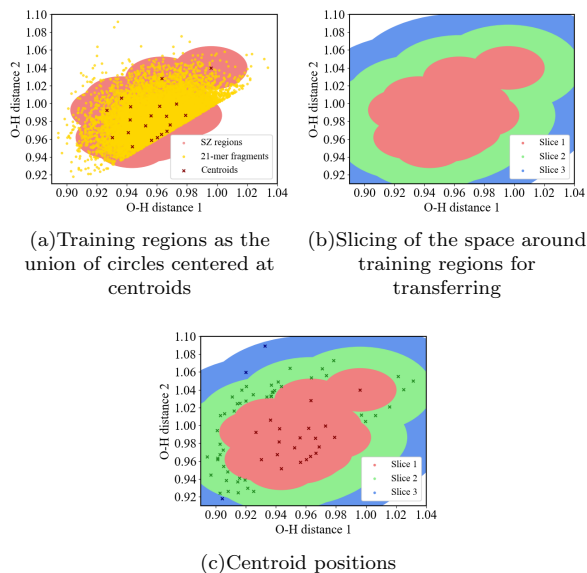


FIG. S7. (a) We place a circle with on each centroid (same as in Figure S5) with radius computed from the maximum sample-to-centroid distance for SZ fragments to define training regions. These regions imply that any data involved can be accurately predicted by SZ models. (b) To include data outside the training regions, we further slice the space based on their distance to the closest centroid and create an incremental transfer process. (c) Centroid positions for slices 2 and 3 are obtained from the recursive mini-batch-k-means.

training in the data space of the fragment geometries, generated using the solvated Zundel AIMD trajectory. The procedure is illustrated through Figures S7. This is achieved by first tessellating the entire data space into a series of slices based on the distance to the closest reference points from the primitive training set (that is one-dimensional partition). For example, in Figure S7(a) and (b), the red region represents the original solvated Zundel water fragments data span (compare with Figure S5). Expanding this space in the 21-mer data space involves creating multiple additional layers or "shells" in that data space surrounding the "solvated Zundel core". The additional slices added incrementally are shown in green and blue in Figure S7(b). These slices facilitate an incremental learning procedure beyond the networks obtained from the solvated Zundel systems based on the proximity of data to inner layers. The slice width is determined from the maximum sample-to-centroid distance from the 10% mini-batch-k-means clustering on the solvated zundel fragments. In Figure S7, the slice width is equal to the radius of the red circles. Following this, for each new slice of the space (that is, for example the green and blue slices in Figure S7), we apply recursive mini-batch-k-means algorithms on geometries within the specific slice to identify a set of geometries

with desired mutual distances to represent the slice of molecular potential energy space. These are now depicted as the new centroids in Figure S7(c). Compare Figure S7 and S5(a) to see how the data space has grown incrementally through this procedure.

To obtain the individual centroids within each additional slice in Figure S7(b), we introduce a recursive mini-batch-k-means procedure. This algorithm intends to divide additional slices of space into pieces at a similar size to those in slice 1. To measure the size of clusters from tessellation, we compute average inertia as the average sample-to-centroid distances. Then we recursively apply mini-batch-k-means on each additional slice of data until the average inertia of each cluster aligns with the average inertia from the slice 1 clusters. A set of centroids is produced as demonstrated in Figure S7(c). The detailed setup and mathematics of the recursive clustering process can be found in Section S4 A.

After identifying the additional centroids using the recursive k-means clustering algorithm, an additional training set is formed from the geometries closest to each centroid to adapt the neural network model. Once the neural networks are trained on the additional training set, they are retrained with geometries closest to all existing centroids as a fine-tuning process. With slicing, the complexity of neural network training is reduced because the transfer process is conducted based on the proximity of the data to the primitive training set. In the next section, we demonstrate how the error changes as we include more slices of data.

#### A. Expanding the domain of training, one slice at a time

When we integrate fragments from different systems and intend to create a single model to represent all of them, the number of fragments obtained from larger systems increases rapidly with system sizes. For efficient additional training set sampling, we slice the data space based on the distance to the nearest primitive training set geometry and develop a recursive mini-batch-k-means procedure to identify the most representative geometries in each slice for transfer learning.

We begin with a primitive neural network model trained on a set of primitive training data, and clustering information comprising sample to centroid distance and inertia from the clustering process. (See the red region in Figure S7(b).) Based on the primitive training data, the entire data space is partitioned into slices determined by the distance to the closest primitive training point. (Illustrated using the green and blue regions in Figure S7(b).) The width of each slice is computed from the maximum sample to the centroid distance from the mini-batch-k-means for the primitive data set (shown in red in Figure S7). Thus, any new incoming data in the space

is given a slice number indicating its distance from primitive training data. The slicing order optimizes memory allocation and computation as the slice numbers indicate a growing distance from primitive (solvated Zundel) training data. Dividing the new data in this manner, that is by using distance from the primitive training set, also provides an ordered transfer learning process, where data is processed based on growing dissimilarity to primitive data. In this manner, we iterate through all slices beginning from the one closest to the primitive set and apply recursive mini-batch-k-means for sampling within each slice.

#### B. The recursive mini-batch-k-means clustering within the slices

The recursive mini-batch-k-means intends to create clusters with sizes approximately the same as those from the 10% mini-batch-k-means on the primitive data (Slice 1). From Ref. [1] and Table S2, we conclude that neural network models trained on the 10% training data, where the training data is obtained from k-means clustering, are highly accurate and represent solvated Zundel potential within sub-kcal/mol accuracy. Based in this training data for the primitive, solvated Zundel data set, we compute the average inertia ( $\eta_0$ ) to measure the average cluster size for the 10% clustering process and use it as the target for additional slices clustering. The average inertia is computed as

$$\eta_0 = \frac{1}{M} \sum_a^k \sum_{m \in C_a} |m - \bar{m}_a|^2 \quad (\text{S14})$$

where  $M$  is the number of primitive data points used for clustering the fragments found in the solvated Zundel trajectory,  $k$  is the number of training data points and also represents the number of k-means clusters or regions into which the  $M$  data points are divided,  $C_a$  are the (irregular and multi-dimensional) regions, and also set of points within the  $a$ -th cluster with  $\bar{m}_a$  being the centroid of the region  $C_a$ .

For example for the  $H_2O$  fragment from within the solvated zundel data as described in Figure S8(a),  $\eta_0$  is computed from the red lines partitioning the space, with the  $\bar{m}_a$  geometries represented as "X". We aim to create similar tessellations for additional slices like those within the green area and blue area in Figure S8(b). We begin with a coarse partitioning of data by using a mini-batch-k-means clustering with the number of clusters chosen as the square root of the number of samples in the slice as shown in Figure S8(c). We label this clustering process as round 1 ( $j = 1$ ) and compute the cluster-wise average inertia similar to Eq. S14 but only for data within the

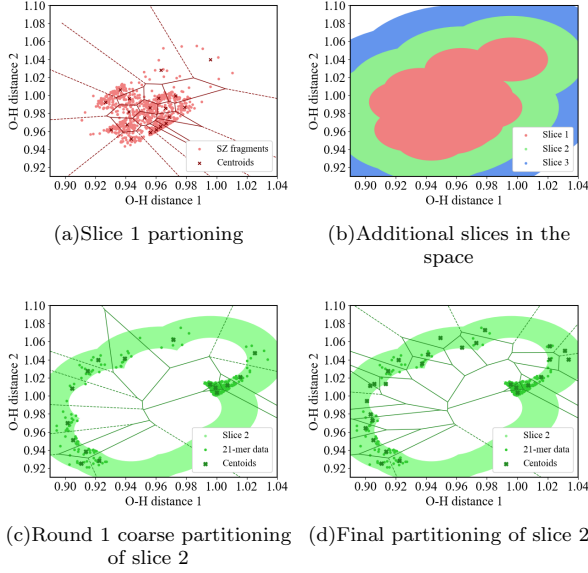


FIG. S8. The process of recursive mini-batch-k-means for additional slices partitioning.

$s$ -th slice,  $l$ -th cluster, iteration round number  $j$  as

$$\eta_{s,j,l} = \frac{1}{M_{s,j,l}} \sum_{m \in C_{s,j,l}} |m - \bar{m}_{s,j,l}|^2. \quad (\text{S15})$$

where  $M_{s,j,l}$  is the number of sample points in the  $s$ -th slice,  $l$ -th cluster, for iteration round number  $j$ . As shown in Figure S8(c), some clusters are too large, such as the top and rightmost. The value of  $\eta_{s,j,l}$  for every cluster is used to measure the size of the cluster and compare it with the target average inertia of  $\eta_0$ . If  $\eta_{s,j,l} > 2 * \eta_0$ , we perform a second round ( $j = 2$ ) of mini-batch-k-means clustering on the data within the  $s$ -th slice,  $l$ -th cluster requiring that the  $l$ -th cluster be further sub-divided into the following number of the cluster:

$$k_{s,j+1,l} = \frac{\eta_{s,j,l}}{\eta_0}. \quad (\text{S16})$$

Then we compute cluster-wise average inertia from Eq. S15 for the round 2 clusters ( $j = 2$ ) and compare their  $\eta_{s,j,l}$  with  $2 * \eta_0$  again. This recursive process continues until all  $\eta_{s,j,l}$  for clusters are below the threshold  $2 * \eta_0$  and ultimately lead to space partitioning shown in Figure S8(d). Here we can clearly see that the large cluster in Figure S8(c) such as the rightmost one is further divided into 4 clusters.

## S5. MINI-BATCH-K-MEANS SAMPLING AND INITIAL NEURAL NETWORK MODEL SETUP

We follow the same process and setting to generate neural network models described in Ref. [1] except that the activation functions on hidden layers have been changed to Gaussian functions. Specifically, to generate the initial neural network model for solvated zundel fragments, we begin by collecting all fragments from the solvated zundel trajectory and create a data bank. For each type of fragment, we use mini-batch-k-means for 10% sampling. The mini-batch-k-means algorithm is a variant of the clustering algorithm k-means clustering, which essentially tessellates or divides the data space into  $k$  mutually exclusive regions called clusters  $\{C_j\}$ . Every cluster is represented by a centroid  $\bar{\mathbf{r}}_j$  which is computed as the arithmetic mean of all data points  $\{\mathbf{r}_i\}$  when these are assigned to the closest centroid. The k-means algorithm aims to find a preset number of centroids or clusters iteratively to minimize the cost function

$$\sum_{j=1}^k \sum_{\mathbf{r}_i \in C_j} |\mathbf{r}_i - \bar{\mathbf{r}}_j|^2. \quad (\text{S17})$$

This cost function computes the total inertia similar to Eq.S14 where we compute the average inertia. The Mini-batch-k-means algorithm provides an efficient approach by using only a random subset of data (known as batch) to update the centroid positions during each iteration. After finding the centroid positions, we construct the primitive training set as the set of closest data points to every centroid

$$\{\mathbf{s}_j\} = \left\{ \mathbf{r}_i \left| \min_{\mathbf{r}_i} |\mathbf{r}_i - \bar{\mathbf{r}}_j| \right. \right\}. \quad (\text{S18})$$

The data points  $\{\mathbf{s}_j\}$  are now the closest data points to each centroid,  $\mathbf{r}_i$  from the closest centroid  $\bar{\mathbf{r}}_j$  and represents our training data points represented below as  $x_{n=0}$ .

In this paper, we place two neural networks in each model as the array and each neural network is configured with 4 hidden layers. Each hidden layer consists of the number of nodes as 4 times the number of features or the number of inter-atomic distances introduced in Section S2B. The activation function on hidden layers has been modified to a Gaussian function

$$x_{n;a} = \exp(-(w_{n-1,n;a} \cdot x_{n-1})^T \cdot (w_{n-1,n;a} \cdot x_{n-1})) \quad (\text{S19})$$

where  $x_{n;a}$  is the  $a$ -th element of the layer vector  $x_n$  and  $w_{n-1,n;a}$  represents the  $a$ -th row of the weight matrix  $w_{n-1,n}$  connecting layers  $n$  and  $n-1$ . The quantity,  $(w_{n-1,n;a} \cdot x_{n-1})$  is the dot product of the  $a$ -th row of the weight matrix  $w_{n-1,n}$  with the vector  $x_{n-1}$  corresponding to the  $n-1$ -th layer. Thus, each hidden layer

vector is an exponent of an element-wise square of the previous layer vector. During the training process, a bias 1 is appended to each vector in  $\{s_j\}$  from Eq. S18 as the inputs for neural networks, and hence

$$x_{n=0} = \begin{bmatrix} s_j \\ 1 \end{bmatrix} \quad (\text{S20})$$

The bias 1 with its associated weights is used for optimizing the positions of gaussian functions during training. The gaussian type function is useful for reducing the long range effect during transferring so that the currently training slice does not interfere much with the previously learned slices of data space.

The neural network model that we used to fit the fragment energy pattern is a neural network array. This array consists of a series of neural networks each of which learns on the cumulative error on predictions from prior neural networks in the series. So that for  $M$  neural networks in the series, the final prediction is

$$\Delta E^{ML} = \sum_m^M \Delta E^{ML,m} \quad (\text{S21})$$

## S6. ADDITIONAL INFORMATION ON RESULTS FROM TRANSFORMATION PLATFORM

### A. Fragment accuracy improvement through the incremental learning process as illustrated by $H_5O_2^+$

Here we choose the fragment  $H_5O_2^+$  as an example to show the effect of our transfer learning process as described above. We begin by illustrating how the protonated 21 water cluster fragments are partitioned into different slices (as per the algorithm described by Figure S8 and Section S4B) and these are shown in the top panel of Figure S9(a), represented by both the green and gray histograms. These histograms depict the same distribution as the blue histogram in the top panel of Figure S6(d), but with a different bin size that corresponds to the slice width as obtained using the algorithm in Section S4B. The slice width, or bin size, is determined from the maximum sample-to-centroid distances from the 10% mini-batch-k-means clustering, identical to the sampling process to generate the primitive training set. This distance approximates the farthest sample that can be accurately predicted by the model, thus serving as a boundary between learned and unlearned regions of the data space. Consequently, we plot the learned regions in green and highlight the space around the training set. The cyan dot plotted with each green bin in Figure S9, top panels, indicates the data in the first slice is predicted from the initial models trained only on the primitive training set from the

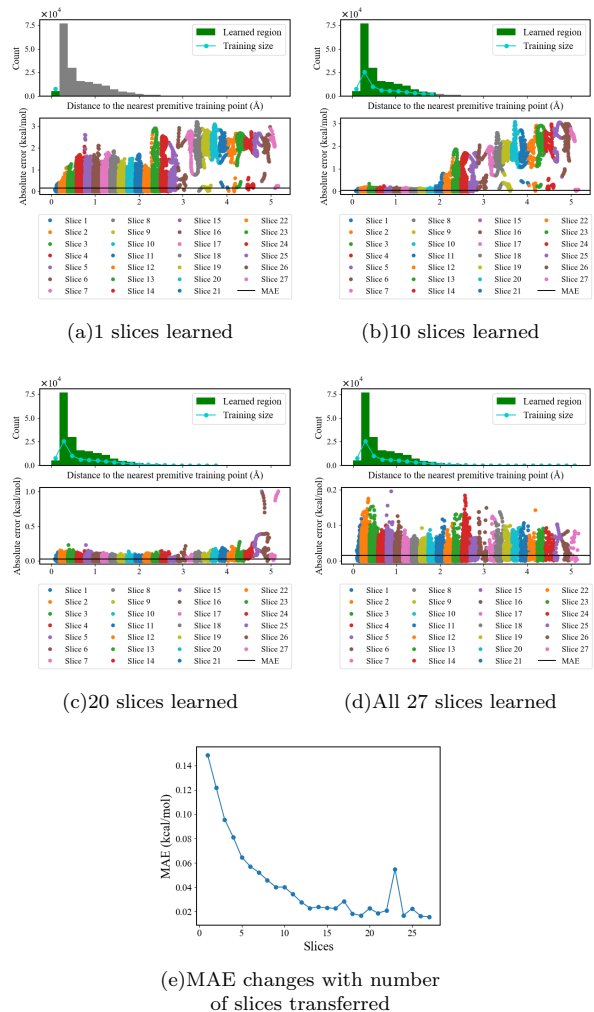


FIG. S9. Error distribution change with the number of slices trained for  $H_5O_2^+$ .

solvated zundel trajectory, the number of training samples exceeds the number of all samples in the slice from the 21-water cluster trajectory. For all subsequent sub-figures, the cyan dots represent the additional training set sizes for each slice of the space. The bottom panel which shares the same horizontal axis as the top one reflects the same error distribution as seen in the middle panel of Figure S6(d), with the space slicing represented by the different colors aligned with each bin in the top panel.

Next, we apply the recursive clustering on protonated 21 water cluster fragments slice by slice, and create an additional training data set as the set of data that are closest to every cluster centroid. Then the neural network models are updated with the additional training set. The training processes incorporate early termina-

tion criteria for negligible improvement in loss function for 20 iterations. Given our approach to transfer slice by slice, the training iterations are significantly reduced. (See Section S4A.) The training and fine-tuning are completed within a few hundred iterations. The changes in error distribution are displayed in Figure S9. As can be seen from Figure S9(b), when the model is transferred to a new slice of the space, the accuracy for the corresponding set of data is significantly improved without affecting much on all previously trained data, hence creating a clear distinction on error distribution between the learned and unlearned regions. The effect is more obvious in Figure S9(c) when we trained for 20 slices of data. When we complete the transferring for all slices, the scale of error distribution is reduced by one order of magnitude as shown in Figure S9(d). The impact of such slice by slice training is given by Figure S9(e), where we demonstrate how the error distribution changes with the addition of slices. Figure S10, S11, S12, S13, S14 complement the discussion above are for the larger clusters.

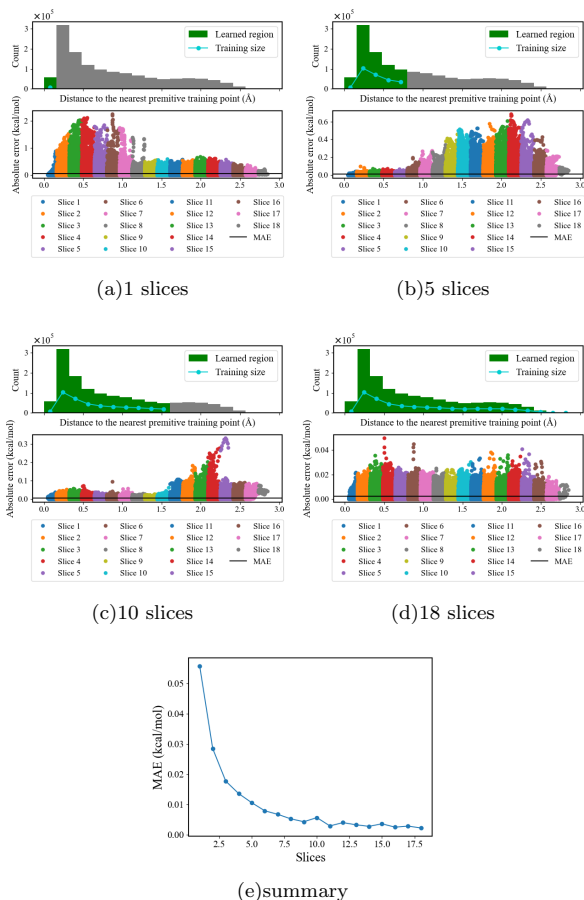


FIG. S10. Error distribution change with number of slices trained for  $H_4O_2$ .

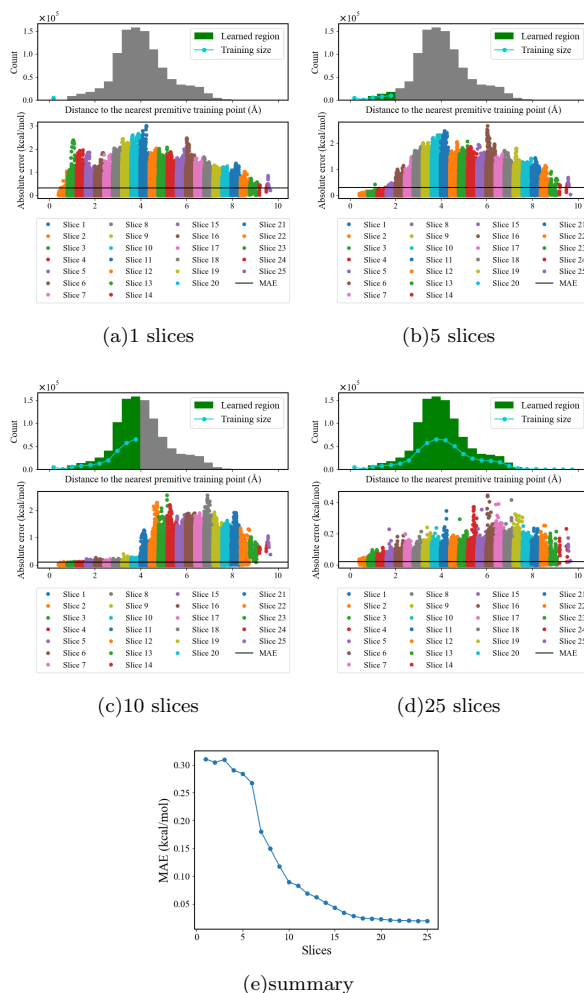


FIG. S11. Error distribution change with number of slices trained for  $H_6O_3$ .

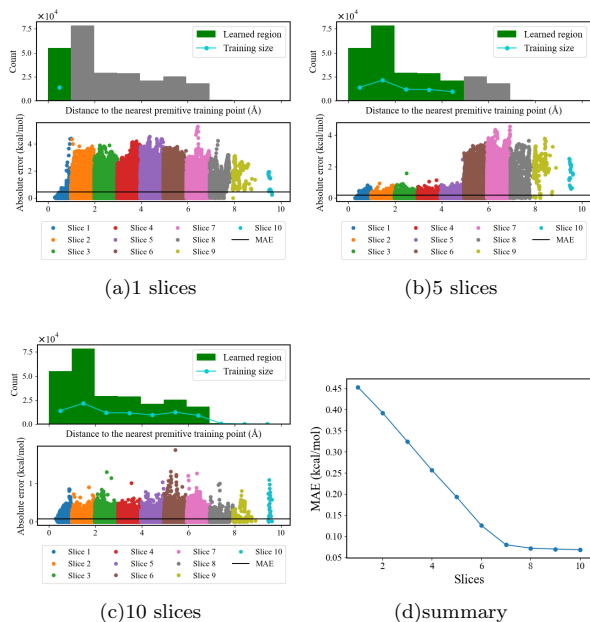


FIG. S12. Error distribution change with number of slices trained for  $H_7O_3^+$ .

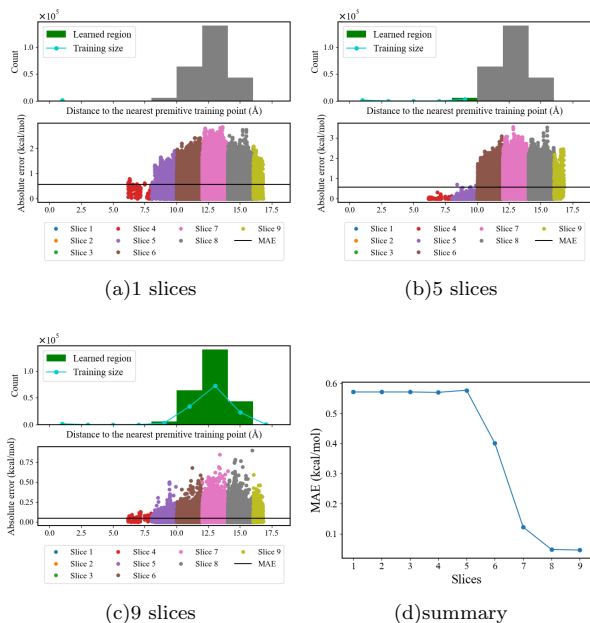


FIG. S13. Error distribution change with number of slices trained for  $H_8O_4^+$ .

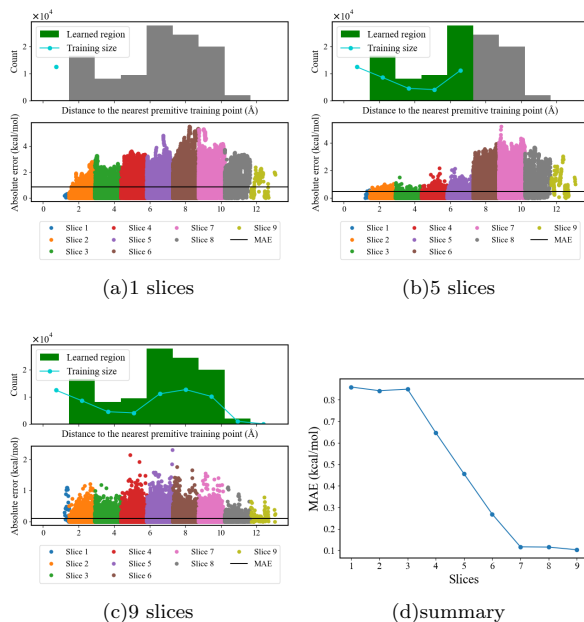


FIG. S14. Error distribution change with number of slices trained for  $H_9O_4^+$ .

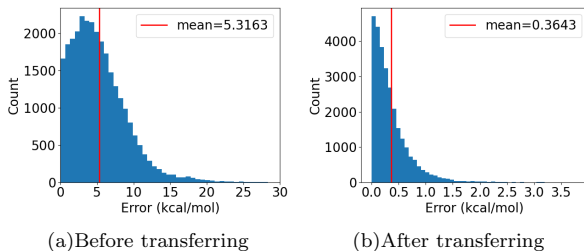


FIG. S15. The protonated 21 water cluster full system potential energy absolute error predicted from models before and after transferring. Subfigure (a) is the same as in Figure S4(b). There are 4 geometries with errors around 120 kcal/mol not shown in this figure. These high errors are due to the doubly protonated water cluster fragments not shown in the solvated zundel trajectories and hence their energy corrections are all predicted as 0 kcal/mol. Due to their low occurrence, these fragments do not affect our test for transferability.

## B. The protonated 21-water cluster and solvated zundel full system accuracy summary

Upon transferring all fragments, we present the protonated 21 water cluster mean absolute error to the target energy in Figure S15 where the error effectively reduced from 5.32 kcal/mol to 0.36 kcal/mol. Additionally, Table S3 provides a summary of all slicing information and

Fragments	primitive training size	Transfer size	MAE before (kcal/mol)	MAE after (kcal/mol)
$H_2O$	3891	~16000	0.00	0.00
$H_3O^+$	1704	~4000	0.00	0.00
$H_4O_2$	6238	~480000	0.06	0.00
$H_5O_2^+$	7751	~76000	0.15	0.02
$H_6O_3$	4694	~470000	0.31	0.02
$H_7O_3^+$	13958	~90000	0.45	0.07
$H_8O_4$	1575	~134000	0.59	0.05
$H_9O_4^+$	12414	~65000	0.88	0.10

TABLE S3. Number of fragments in the protonated 21 water cluster trajectory used for transferring and the fragment mean absolute errors after transferring. Mean absolute errors are rounded to 2 decimal places.

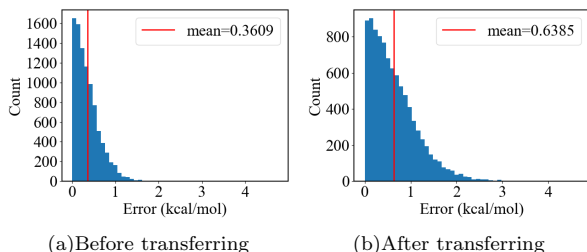


FIG. S16. Solvated zundel full system potential energy absolute error before and after transferring.

fragment accuracy. The transferring process reduces the errors of all protonated 21 water cluster fragments by one order of magnitude.

After transferring, the neural network models are well adapted to fragments from protonated 21 water clusters and produce accurate full system potential energy predictions. The next question we address is how well these models predict the solvated zundel full system. That is, does our retraining preserve the accuracy within the original dataset? This is an important question, since, as can be seen from Figure S9, the dataset size of fragments within the 21-mer dataset is orders of magnitude greater than that from the solvated Zundel data. We show the full system predictions in Figure S16 before and after transferring for comparison. Although the mean absolute error for solvated zundel has grown from 0.36 to 0.64 kcal/mol, the predictions remain accurate for such a physically meaningful subset of all fragments. This shows the robustness of the transferring process and opens a possible approach to incorporate multiple systems and create more general models to access larger problems, while also retaining accuracy on the smaller, learned datasets.

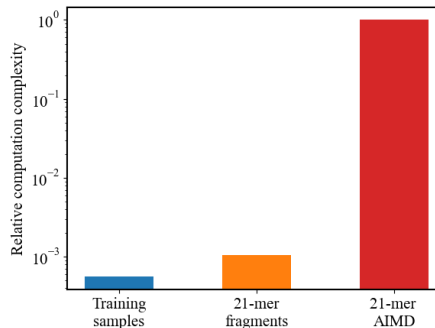


FIG. S17. The relative computational complexity comparison following the complexity of CCSD at  $O(N^6)$  for  $N$  electrons in each system. Training samples shown by the orange bar involve both primitive and additional training sets. Fragments shown by the green bar are produced from both solvated zundel and protonated 21-water cluster trajectories.

### S7. COST OF CONSTRUCTING AND MODIFYING NEURAL NETWORK MODELS BASED ON THE GRAPH THEORETIC METHOD

Here we summarize the total cost for constructing neural network potential energy surfaces for both the solvated zundel and the protonated 21-water cluster. The final training set, comprising both the initial and additional training set, represents 32% of fragment geometries obtained from both trajectories. We approximate the computational cost for potential energies as  $N^6$  for  $N$  electrons following the scaling of CCSD. Thus as shown by the red bar in Figure S17, the protonated 21-water cluster trajectory which contains 28294 frames of 211-electron geometries has a total cost of  $2.5 \times 10^{18}$  and normalized as 1. In contrast, the total cost for all fragments (42 electrons at most) produced from the same trajectory is only about  $2.6 \times 10^{15}$  as shown by the orange bar. Therefore, the graph-theoretic fragmentation process reduces the computational cost by 3 orders of magnitude.

According to our estimation in earlier sections (S1), constructing a neural network model for a potential energy surface would require  $(3N-6)^2$  training samples for  $N$  atoms. Without fragmentation, a model for a 21-mer potential energy surface would require over 30 thousand training samples to model the 186-dimensional surface. By using fragmentation, we need only around one-third

of the fragments from 30 thousand 21-mer geometries. Given that these fragments are 3 orders of magnitude cheaper to compute than the full system, our graph-theoretic neural network modeling achieves an overall reduction of more than 3 orders of magnitude in training sample cost for modeling potential energy surfaces.

- 
- [1] Zhu, X.; Iyengar, S. S. Graph Theoretic Molecular Fragmentation for Multidimensional Potential Energy Surfaces Yield an Adaptive and General Transfer Machine Learning Protocol. *J. Chem. Theory Comput.* **2022**, *18*, 5125–5144.
- [2] Ricard, T. C.; Zhu, X.; Iyengar, S. S. Capturing weak interactions in surface adsorbate systems at coupled cluster accuracy: a graph-theoretic molecular fragmentation approach improved through machine learning. *J. Chem. Theory Comput.* **2023**, *19*, 8541.
- [3] Schran, C.; Behler, J.; Marx, D. Automated Fitting of Neural Network Potentials at Coupled Cluster Accuracy: Protonated Water Clusters as Testing Ground. *J. Chem. Theory Comput.* **2020**, *16*, 88–99.
- [4] Nguyen, T. T.; Szekely, E.; Imbalzano, G.; Behler, J.; Csanyi, G.; Ceriotti, M.; Goetz, A. W.; Paesani, F. Comparison of permutationally invariant polynomials, neural networks, and Gaussian approximation potentials in representing water interactions through many-body expansions. *J. Chem. Phys.* **2018**, 148.
- [5] Lu, F.; Cheng, L.; DiRisio, R. J.; Finney, J. M.; Boyer, M. A.; Moonkaen, P.; Sun, J.; Lee, S. J. R.; Deustua, J. E.; Miller, T. F., III; McCoy, A. B. Fast Near Ab Initio Potential Energy Surfaces Using Machine Learning. *J. Phys. Chem. A* **2022**, *126*, 4013–4024.
- [6] Law, M. M.; Fraser-Smith, J. T.; Perotto, C. U. The potential energy surface of isomerising disilyne. *PHYSICAL CHEMISTRY CHEMICAL PHYSICS* **2012**, *14*, 6922–6936.
- [7] Castro, E.; Avila, G.; Manzhos, S.; Agarwal, J.; Schaefer, H. F.; Carrington, T., Jr. Applying a Smolyak collocation method to  $C_2CO$ . *MOLECULAR PHYSICS* **2017**, *115*, 1775–1785.
- [8] Iyengar, S. S.; Ricard, T. C.; Zhu, X. A reformulation of all ONIOM-type molecular fragmentation approaches using graph theory-based projection operators: Applications to dynamics, molecular potential surfaces, and machine learning and quantum computing. *J. Phys. Chem. A* **2024**, *128*, 466.
- [9] Björklund, A.; Husfeldt, T.; Koivisto, M. Set Partitioning via Inclusion Exclusion. *SIAM J. Comput.* **2009**, *39*, 546.
- [10] Zhang, J. H.; Iyengar, S. S. Graph- $|Q\rangle\langle C|$ : A Graph-based Quantum-classical algorithm for efficient electronic structure on hybrid quantum/classical hardware systems: Improved quantum circuit depth performance. *J. Chem. Theory Comput.* **2022**, *18*, 2885.
- [11] Iyengar, S. S.; Zhang, J. H.; Saha, D.; Ricard, T. C. Graph- $|Q\rangle\langle C|$ : A Quantum Algorithm with Reduced Quantum Circuit Depth for Electronic Structure. *J. Phys. Chem. A* **2023**, *127*, 9334.
- [12] Dey, T. K.; Shah, N. R. On the number of simplicial complexes in Rd. *Comput. Geom.* **1997**, *8*, 267.
- [13] Adams, C. C.; Franzosa, R. D. Introduction to topology: pure and applied; 2008.
- [14] Berger, M.; Pansu, P.; Berry, J.-P.; Saint-Raymond, X. Affine spaces. In *Problems in Geometry*; Springer, 1984; p 11.
- [15] Li, J.; Iyengar, S. S. Ab initio Molecular Dynamics using Recursive, Spatially Separated, Overlapping Model Subsystems Mixed Within an ONIOM Based Fragmentation Energy Extrapolation Technique. *J. Chem. Theory Comput.* **2015**, *11*, 3978–3991.
- [16] Li, J.; Haycraft, C.; Iyengar, S. S. Hybrid, Extended Lagrangian – Born-Oppenheimer *Ab Initio* Molecular Dynamics using Fragment-Based Electronic Structure. *J. Chem. Theory Comput.* **2016**, *12*, 2493.
- [17] Haycraft, C.; Li, J.; Iyengar, S. S. Efficient, “On-the-fly” Born–Oppenheimer and Car–Parrinello–type Dynamics with coupled cluster accuracy through Fragment Based Electronic Structure. *J. Chem. Theory Comput.* **2017**, *13*, 21887.
- [18] Ricard, T. C.; Haycraft, C.; Iyengar, S. S. Adaptive, geometric networks for efficient coarse-grained *ab initio* molecular dynamics with post-Hartree-Fock accuracy. *J. Chem. Theory Comput.* **2018**, *14*, 2852.
- [19] Ricard, T. C.; Iyengar, S. S. Efficiently capturing weak interactions in *ab initio* molecular dynamics through “on-the-fly” basis set extrapolation. *J. Chem. Theory Comput.* **2018**, *14*, 5535.
- [20] Kumar, A.; Iyengar, S. S. Fragment-based electronic structure for potential energy surfaces using a superposition of fragmentation topologies. *J. Chem. Theory Comput.* **2019**, *15*, 5769.
- [21] Ricard, T. C.; Iyengar, S. S. An efficient and accurate approach to estimate hybrid functional and large basis set contributions to condensed phase systems and molecule-surface interactions. *J. Chem. Theory Comput.* **2020**, *16*, 4790.
- [22] Ricard, T. C.; Kumar, A.; Iyengar, S. S. Embedded, graph-theoretically defined many-body approximations for wavefunction-in-DFT and DFT-in-DFT: Applications to gas- and condensed-phase *ab initio* molecular dynamics, and potential surfaces for quantum nuclear effects. *Int. J. Quantum Chem.* **2020**, *120*, e26244.
- [23] Kumar, A.; DeGregorio, N.; Iyengar, S. S. Graph-Theory-Based Molecular Fragmentation for Efficient and Accurate Potential Surface Calculations in Multiple Dimensions. *J. Chem. Theory Comput.* **2021**, *17*, 6671–6690.



- [24] Zhang, J. H.; Ricard, T. C.; Haycraft, C.; Iyengar, S. S. Weighted-Graph-Theoretic Methods for Many-Body Corrections within ONIOM: Smooth AIMD and the Role of High-Order Many-Body Terms. *J. Chem. Theory Comput.* **2021**, *17*, 2672–2690.
- [25] Kumar, A.; DeGregorio, N.; Ricard, T.; Iyengar, S. S. Graph-Theoretic Molecular Fragmentation for Potential Surfaces Leads Naturally to a Tensor Network Form and Allows Accurate and Efficient Quantum Nuclear Dynamics. *J. Chem. Theory Comput.* **2022**, *18*, 7243.
- [26] Maseras, F.; Morokuma, K. IMOMM: A new integrated ab initio + molecular mechanics geometry optimization scheme of equilibrium structures and transition states. *J. Comput. Chem.* **1995**, *16*, 1170.
- [27] Hartigan, J. A.; Wong, M. A. Algorithm AS 136: A k-means clustering algorithm. *J. R. Stat. Soc. series c (applied statistics)* **1979**, *28*, 100–108.